A&A, 710, A294 (2026)
https://doi.org/10.1051/0004-6361/202659085
© The Authors 2026

Astronomy & Astrophysics

Gaia20fnr: A binary-lens microlensing event with full orbital motion revealed by four space telescopes

M. Wicker[1,2,⋆], Ł. Wyrzykowski[1,3], M. Hundertmark[4], K. A. Rybicki[1], P. Zieliński[5], E. Stonkutė[6], M. Gromadzki[1], M. Maskoliūnas[6], N. Ihanec[2], M. Ratajczak[1], E. Bachelet[7], K. Kruszyńska[8], M. Dominik[9], D. A. H. Buckley[10,11], I. Gezer[12], A.-N. Chené[13], P. Mikołajczyk[3,14], K. Kotysz[1,14], J. Majumdar[1], E. Pakštienė[6], J. Zdanavičius[6], V. Čepas[6], U. Jonauskaitė[6]
V. Bozza[15,16], A. Cassan[17], R. Figuera Jaimes[18,19], M. Rabus[20], P. Rota[15,16], R. A. Street[8], Y. Tsapras[4], J. Wambsganss[4] (The OMEGA Key Project)
S. Awiphan[21], S. M. Brincat[22], Z. Budzik[1], J. W. Davidson Jr.[23], R. Dymock[24], C. Galdies[25,26], V. Godunova[27], F.-J. Hambsch[28,29], M. Jabłonska[1,30], P. Kowalik[31], T. Kvernadze[32], M. Larma[33,34], M. Makowska[35], Y. Markus[36,27], J. Merc[37,38], O. Michniewicz[39], M. Motylinski[5], A. Popowicz[31], M. Radziwonowicz[1], D. Reichart[40], F. D. Romanov[41], A. O. Simon[42,43], P. Trzcionkowski[1], E. Wróbel[31], M. Zejmo[39], and S. Zola[44] (BHTOM Observers)

(Affiliations can be found after the references)

Received 22 January 2026 / Accepted 26 April 2026

ABSTRACT

The microlensing event Gaia20fnr is a long-duration, non-caustic-crossing binary-lens event located at a high Galactic latitude. Triggered by a photometric rise detected by the Gaia space mission, the event was followed up with observations from multiple ground-based facilities and observed by four space telescopes: Gaia, NEOWISE, Swift, and TESS. We characterised the Gaia20fnr microlensing system by determining the physical and orbital properties of the binary lens, the nature of the luminous source, and the kinematics of both the source and the lens. We employed a binary-lens microlensing model including full Keplerian orbital motion and annual microlens parallax to fit the photometric data. The event is best explained by a K2 giant source at $D_S = 3.10 \pm 0.10$ kpc lensed by a stellar binary composed of $M_{L,1} = 0.46 \pm 0.06\,M_\odot$ and $M_{L,2} = 0.52 \pm 0.06\,M_\odot$ at a distance of $D_L = 0.54 \pm 0.05$ kpc. The light curve exhibits strong signatures of orbital motion and requires a full Keplerian model with a period of $P = 0.67 \pm 0.04$ yr and a predicted semi-amplitude of $K_1 = 16.9 \pm 0.9\,\mathrm{km\,s^{-1}}$. Gaia20fnr is one of the few microlensing events for which a complete Keplerian binary-lens solution has been derived. The model may be further constrained with the forthcoming Gaia DR4 and DR5 astrometric time-series data, while high-angular-resolution imaging and radial-velocity follow-ups could become feasible once the source and lens are sufficiently separated, despite the observational challenges posed by the bright source. Its long duration, multi-peak structure, and extensive coverage from both space- and ground-based facilities make it a benchmark for studying faint nearby low-mass binaries through microlensing.

Key words. gravitational lensing: micro – astrometry – celestial mechanics – binaries: general

1. Introduction

Binary star systems are key to understanding stellar astrophysics. They provide measurements of stellar masses and luminosities, which strongly constrain the mass–luminosity relation and models of stellar evolution (Paczyński 1971; Boffin & Jones 2024). Studies of stellar binaries have typically relied on direct measurements of light emitted by the binary system, such as radial velocities, to determine the mass and interaction between bodies (Popper 1967; Torres et al. 2010). These traditional techniques are restricted to a small and systematically biased subset of binary systems, as precise dynamical solutions require bright systems with well-measured radial-velocity curves and, ideally, eclipses. As a result, samples with accurately known masses and radii remain small and strongly biased towards nearby, relatively unevolved, and non-interacting systems (Torres et al. 2010; Morales et al. 2022). Population studies further show that a large fraction of binaries (especially long-period systems, low-mass companions, and systems containing compact remnants) remain essentially unconstrained by direct light and radial-velocity measurements. This leads to severe selection effects in inferred binary demographics (Moe & Di Stefano 2017; Casares & Jonker 2014). Alternative detection techniques are essential because these selection effects leave large portions of the binary parameter space unexplored.

In 1986, Bohdan Paczyński proposed gravitational microlensing as a method to detect compact dark matter objects, such as massive compact halo objects (MACHOs), in the Galactic halo by observing their lensing effects on background stars (Paczynski 1986; Alcock et al. 1996). Since

⋆ Corresponding author: mwicker@astrouw.edu.pl

Open Access article, published by EDP Sciences, under the terms of the Creative Commons Attribution License (https://creativecommons.org/licenses/by/4.0), which permits unrestricted use, distribution, and reproduction in any medium, provided the original work is properly cited.
This article is published in open access under the Subscribe to Open model. Subscribe to A&A to support open access publication.

then, gravitational microlensing has proven to be an effective method for detecting isolated and otherwise hard-to-find objects such as planetary systems (e.g. Bond et al. 2004; Beaulieu et al. 2006; Bennett et al. 2016) free-floating or wide-orbit planets (e.g. Mróz et al. 2018, 2019; Poleski et al. 2021; Dong et al. 2026), and stellar-mass black holes (Sahu et al. 2022; Lam et al. 2022). These studies have provided estimates and constraints for stellar, planetary, and dark remnant populations (e.g. Wyrzykowski et al. 2016; Sweeney et al. 2024; Kruszyńska et al. 2024; Abrams et al. 2025; Kaczmarek et al. 2025; Mróz et al. 2025) as well as explanations for complex, multi-peak microlensing light curves that are difficult to explain using simpler lens models or other astrophysical sources of variability (e.g. Udalski et al. 2018; Wyrzykowski et al. 2020). Gravitational microlensing has proven particularly powerful for discovering and characterising binary systems that are faint, distant, or characterised by significant orbital motion (e.g. Skowron et al. 2011; Penny et al. 2011b).

Large microlensing surveys (e.g. OGLE (Udalski et al. 1997); MOA (Bond et al. 2001); KMT (Kim et al. 2016); PRIME (Sumi et al. 2025)) typically target regions of high stellar density, such as the Galactic bulge and Magellanic Clouds, to maximise the event rate. While these surveys rely on monitoring dense stellar fields from the ground, the Gaia mission provides an entirely different and complementary approach to microlensing discovery. Operating from space, Gaia has conducted an all-sky high-precision astrometric and photometric survey of the entire sky. As a result, Gaia is sensitive to microlensing events across the entire sky, including regions that are sparsely or not at all monitored by traditional ground-based programmes. This makes Gaia uniquely valuable for uncovering objects acting as gravitational lenses that could otherwise be underrepresented, such as nearby lenses and high proper-motion objects. The first catalogue of Gaia microlensing events was presented in Wyrzykowski et al. (2023) as part of Gaia Data Release 3 (DR3).

To make use of transients observed by Gaia and to enable timely follow-up observations, the Gaia Science Alerts (GSA; Hodgkin et al. 2021) system identifies transient brightness variations in real time. This has enabled the coordination of fast follow-up observations for a variety of transients. Follow-up observations, both photometric and spectroscopic, have produced results of GSA for a variety of sources, such as eclipsing AM CVn-systems (e.g. Campbell et al. 2015), superluminous supernovae (e.g. Kangas et al. 2017; Nicholl et al. 2017), nuclear transients (e.g. Kostrzewa-Rutkowska et al. 2018; Pessi et al. 2025), cataclysmic and symbiotic variables (e.g. Merc et al. 2020; Mistry et al. 2022; Merc et al. 2024), electromagnetic counterparts to gravitational-wave observations (e.g. Kostrzewa-Rutkowska et al. 2020), and gravitational microlensing events (e.g. Rybicki et al. 2022; Wyrzykowski et al. 2020; Kruszyńska et al. 2022; Pylypenko et al. 2026).

Gaia's forthcoming Data Release 4 (DR4), expected in December 2026, will include full astrometric time-series data for all sources with epoch-by-epoch centroid positions rather than only the five-parameter average solutions of previous releases. Astrometric microlensing modelling will allow for direct measurement of the lens mass and distance (Jankovič et al. 2025). The joint astrometric and photometric data will be key in breaking the degeneracies inherent in photometric-only microlensing observations and will challenge current results derived from photometric models.

Population studies show that approximately 5–10 % of microlensing events exhibit signatures of binary lenses (Mao & Paczynski 1991; Udalski et al. 2000; Dominik 2006; Oliveira et al. 2025). In contrast to single-lens events, which produce a simple symmetric light curve, binary lenses can generate complex caustic structures that depend sensitively on the mass ratio and projected separation of the components (Bozza 2001; Rattenbury et al. 2002; Cassan 2008). These caustic networks produce sharp, high-magnification features that can tightly constrain lens geometry when the photometric coverage densely samples caustic crossings or cusp approaches, where the magnification pattern is particularly sensitive to binary geometry (Jaroszyński & Mao 2001; Skowron et al. 2007). In addition to the standard binary-lens parameters, higher order effects are often required to obtain physical solutions. These include microlens parallax, caused by the observer's motion around the Sun or by observations from separated observatories, and finite-source effects associated with limb-darkened source profiles. Together, these effects break degeneracies and permit measurements of the lens mass and distance (Witt & Mao 1994; Gould 2004). Incorporating these effects increases model complexity but is essential for converting microlensing observables into robust physical parameters (Bennett et al. 2007; Dong et al. 2009). For binary-lens microlensing events, higher order effects from orbital motion can produce time-varying caustic structures that substantially alter the resulting light curve.

Wide binaries of low-mass (solar-type) stars typically have orbital periods of the order of a few hundred years (Raghavan et al. 2010), far exceeding the Einstein crossing time, t_E, of most microlensing events. In contrast, close binaries, such as massive-star pairs or post-common-envelope systems, can have orbital periods, P, comparable to or shorter than t_E. In general, for binary lenses with $P \gg t_E$, orbital motion can be neglected in microlensing models (Penny et al. 2011b; Di Stefano & Esin 2014). However, when $P \lesssim t_E$, orbital evolution can significantly alter the projected separation and orientation of the lens components, thereby modifying the caustic morphology and producing measurable deviations in the light curve relative to static binary-lens models, which can no longer provide satisfactory fits (Albrow et al. 2000; Nucita et al. 2014; Guo et al. 2015). Notably, Shin et al. (2012) found that systems with $P \sim 1$–3 yr could not be satisfactorily modelled without including orbital motion, even though their periods exceeded typical t_E values. Long event timescales and the proximity to resonant caustic configurations render light curves sensitive to small changes in the projected binary geometry.

Although rotating binary stars increase the complexity of the microlensing model, the corresponding Keplerian orbital parameters (period, velocity amplitude, eccentricity, phase, and position of periapsis) provide an independent means of testing the model via radial-velocity measurements. This possibility was demonstrated for the OGLE-2009-BLG-020 event, where the prediction of Skowron et al. (2011) was subsequently verified through radial-velocity measurements by Yee et al. (2016).

Here, we present a detailed analysis of a unique microlensing event characterised by significant binary orbital motion and no caustic-crossing features, Gaia20fnr. This event provides a rare opportunity to constrain the orbital parameters of the binary lens system, characterised by its five Keplerian parameters. The photometric event lasted for over a year, with multiple distinct features in the light curve. Apart from a short period before the maximum magnification where the event was unobservable because of the proximity of the Sun to the line of sight of the microlensing event, the event was observed for the entirety of the source magnification, with ample photometric data at the baseline before and after the source magnification. Due to an early alert from Gaia, a large network of ground-based telescopes

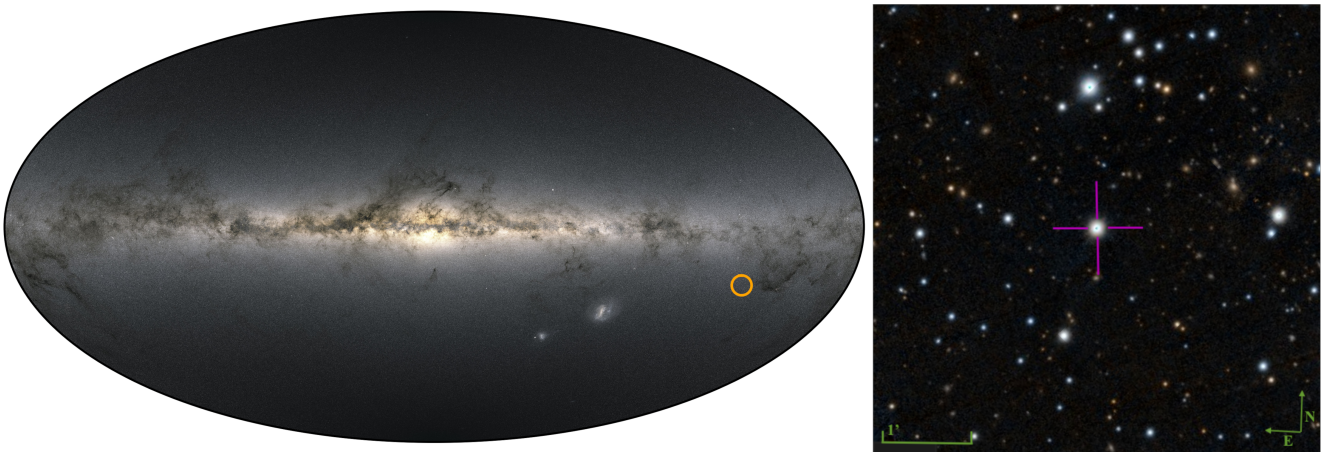


Fig. 1. Sky map view of the Milky Way with the location of Gaia20fnr marked with an orange circle. This illustrates the unique location of the microlensing event. The figure was made with `MW-Plot` and Gaia EDR3 data (Gaia Collaboration 2021). On the right, a finding chart made from Pan-STARRS1 (Chambers et al. 2019) data via the `ALADIN` Tool (Bonnarel et al. 2000).

coordinated by the Black Hole Target and Observation Manager (BHTOM[1]) (Wyrzykowski 2024; Mikolajczyk et al. 2025) was able to observe the event in a variety of filters. BHTOM facilitates coordinated observations and the processing of photometric time-series data, building on the open-source TOM Toolkit developed at Las Cumbres Observatory (LCO; Street et al. 2018, 2024b). The high cadence of observations, especially during each of the three magnification periods, enabled us to find a unique solution with well-constrained parameters for a single source and a rotating binary lens. The detailed modelling presented here aims not only to impose lens mass estimates but also to provide robust parameters that can be independently verified by subsequent radial-velocity and astrometric data, mirroring the approaches demonstrated by Skowron et al. (2011) and Wyrzykowski et al. (2020).

The structure of this paper is as follows. In Sections 2 and 3, we detail the Gaia alert, the photometric data, and the spectroscopic observations. Sections 4 and 5 outline the microlensing modelling, particularly emphasising the incorporation of orbital motion to model the data and the physical parameters of the source and lens. The results are discussed in Section 6.

2. Discovery and photometric follow-up

The Gaia20fnr microlensing event (IAU designation AT2020ably in the Transient Name Server), located at equatorial coordinates $(\alpha, \delta)_{J2000} = \left(06^{\rm h}01^{\rm m}04.08^{\rm s}, -18°58'03.72''\right)$, was identified as a transient event by GSA[2] on 2 December 2020 (Hodgkin et al. 2020). The Galactic coordinates of the event are $(l, b) = (224.878°, -19.372°)$, such that Gaia20fnr is in a region of the Milky Way with low stellar density and far from the Galactic bulge and disk. The finding chart and sky location of Gaia20fnr are shown in Fig. 1.

The Gaia DR3 catalogue (Gaia Collaboration 2023b) source parameters for the alerted Gaia object are listed in Table 1. The source also has a counterpart in the Two Micron All Sky Survey (2MASS; Skrutskie et al. 2006) as 2MASS 06010409-1858038. The alert was issued following a 0.26 mag rise in the Gaia G band relative to five years of pre-alert observations, during which the source had a stable mean magnitude of 13.17 mag (σ = 0.02 mag). Equal magnification in the Gaia blue (BP) and red (RP) bands indicated an achromatic brightening consistent with microlensing. This motivated an extensive follow-up campaign.

Table 1. Gaia DR3 source parameters for Gaia20fnr.

Gaia Source ID	2990431491637998848
(RA, Dec) (deg)	(90.27, −18.97)
(l, b) (deg)	(224.88, −19.37)
ϖ (mas)	0.29 ± 0.01
$\mu_{\alpha*}$ (mas yr^{-1})	−2.25 ± 0.01
μ_δ (mas yr^{-1})	2.72 ± 0.01
m_G (mag)	13.106 ± 0.003
m_{BP} (mag)	13.646 ± 0.003
m_{RP} (mag)	12.413 ± 0.004
RUWE	1.026

The source has historically been observed by a multitude of surveys and in a variety of filters. Such data, obtained before, during, and after the magnification of the source, are crucial for modelling and accurately identifying source and blend fluxes, as they provide a baseline measure of the unmagnified source flux. Additionally, to rule out causes besides microlensing and to determine potential periodic variations/oscillations, historic and continuous observations are vital. The Catalina Real-Time Transient Survey (Drake et al. 2009, 2012) observed the source for a 10-year period from 2005 and shows no significant variability. The Galaxy Evolution Explorer (GALEX; Martin et al. 2005) space telescope observed the source in 2007 with its far ultraviolet (FUV) and near ultraviolet (NUV) filters. The Palomar Transient Factory (PTF) (Law et al. 2009) observed the source between 2009 and 2012 in the R band. The Panoramic Survey Telescope and Rapid Response System (PS1) (Chambers et al. 2019) provided data recorded between 2011 and 2013 in the g, r, i, and z bands. Since November 2013, the All-Sky Automated Survey for Supernovae (ASAS-SN) (Kochanek et al. 2017) has been observing the source and continued to observe it for the entire microlensing event. The relatively high cadence of two to five days in the V and g bands results in extensive observational coverage. The Zwicky Transient Facility (ZTF) (Bellm et al. 2019) observed the target in the r and g bands since

[1] https://bhtom.space
[2] https://gsaweb.ast.cam.ac.uk/alerts/alert/Gaia20fnr/

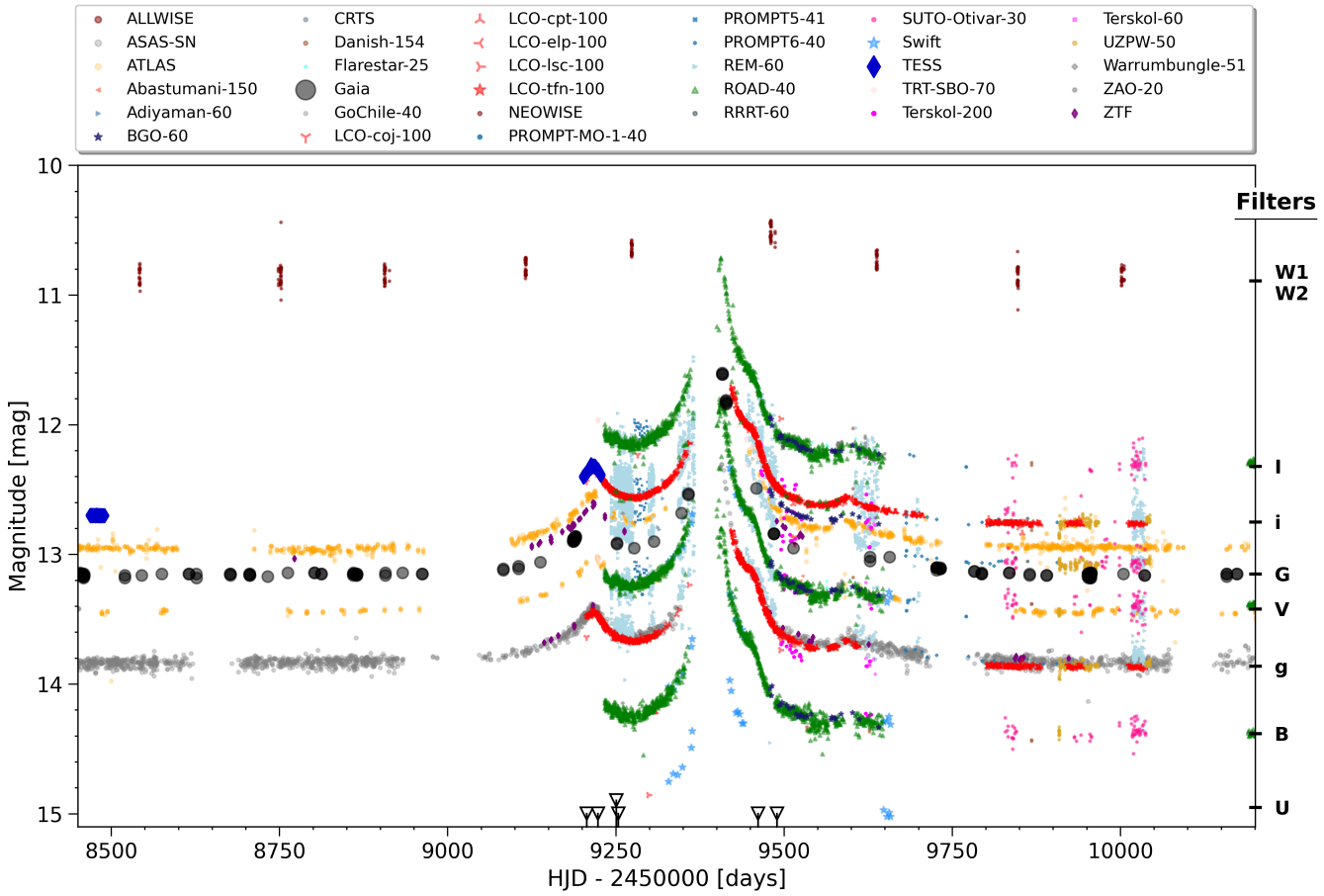


Fig. 2. Photometric observations of Gaia20fnr combining space-based observations, survey data, and follow-up observations gathered by BHTOM. The plotted measurements are calibrated magnitudes in their respective filters, so the vertical offsets between the datasets reflect the different passbands and corresponding magnitude zero points. The Swift UV data in the UVW1 and UVW2 filters are not shown for visibility reasons. These observations were obtained at the same epochs as the Swift U-band data, but have magnitudes higher by 1.6 mag and 2.8 mag in UVW1 and UVW2, respectively. The inverted triangles along the x-axis indicate the epochs at which the spectra were obtained.

November 2018. The ZTF data cover the baseline before magnification, the first peak, the dimming phase following the main peak, and the post-event baseline of the photometrically observable microlensing event. The Asteroid Terrestrial-impact Last Alert System (ATLAS) (Tonry et al. 2018) has been monitoring the source since 2015, providing coverage of the microlensing event with a cadence of roughly four days in the cyan and orange bands.

In addition to Gaia, this event was monitored by three other space-based observatories. Together, these facilities provided coverage from the infrared to the ultraviolet, making the dataset unique for a microlensing event. The Transiting Exoplanet Survey Satellite (TESS) (Ricker et al. 2015) observed the source during three sectors beginning in December 2018, December 2020, and December 2024, with respective time spans of approximately 22, 26, and 27 days. Complementary infrared observations have been obtained since March 2010 by NEOWISE (Mainzer et al. 2011), while ultraviolet monitoring has been provided since April 2021 by the Swift UV/Optical Telescope (Roming et al. 2005).

Following the alert from Gaia, photometric follow-up observations were performed by a large number of telescopes in a variety of visible bands. The observations for this event[3] were collected, and more recently also coordinated, by the BHTOM network of telescopes. Twenty-three different ground-based telescopes provided follow-up observations for five Johnson-Cousins (JC; Bessell (1990)) and five Sloan Digital Sky Survey (SDSS) (Fukugita et al. 1996) filters.

The collection of photometric data, shown for each telescope, is in Fig. 2. The ground-based telescopes that provided photometric follow-up observations are detailed in Table A.1 and details of all photometric observations are listed in Table A.2.

2.1. Gaia photometry

An alert was issued for the Gaia20fnr microlensing event in 2020, with the closest approach between the lens and the source occurring in 2021, and the return to the baseline at the end of 2022. Gaia DR4 will contain data from observations between July 2014 and January 2020, which only covers the first peak of the photometric microlensing event. Only Gaia Data Release 5 (DR5), which is not expected before the end of 2030, will contain the full light curve and also the full astrometric time series. Full and up-to-date photometric G-band observations by the Gaia telescope are published by the GSA system. These, however, do not provide magnitude errors for published events. To estimate these error bars, we followed the method of Kruszyńska et al. (2022).

[3] https://bhtom.space/public/targets/Gaia20fnr

2.2. Ground-based follow-up

The Gaia20fnr alert came more than 200 days before the closest approach between the source and the lens. This has enabled an extensive photometric follow-up campaign to collect data for the majority of the event, covering almost all features in their entirety. The very first photometric follow-up observations started 20 days after the alert was issued, on 22 December 2020, by the OMEGA Project, using the LCO Global Telescope Network of 1-m telescopes (Brown et al. 2013). LCO data in the g and i bands were obtained using the 1-m Sinistro-camera telescopes located in Australia, Chile, South Africa, Tenerife, and the USA.

Because of the event's position on the sky relative to the Sun, it was unobservable from Earth for a period leading up to the main peak. Nevertheless, observations from the BHTOM observers, specifically the ROAD observatory (Hambsch 2012), pushed the observing limits and captured much of the peak, which was critical for constraining the model parameters and for potentially detecting finite-source effects. On 7 October 2021, almost a year after the alert of the transient event, the object reached its peak magnitude of $m_V = 11.8$ mag. The third and smallest brightening phase in January 2022 was extensively observed and was crucial in constraining the orbital motion parameters despite its relatively small magnification of 1.2 times the baseline source flux (compared to 1.5 for the first and 4.35 for the second peak).

All of the ground-based photometric observations were processed using the BHTOM tool, an automated system designed for managing the targets and processing of the time-domain data. Bias-, dark-, and flat-field-corrected images were analysed to extract instrumental photometry for all detected stars using the package CCDPhot built into BHTOM. The resulting photometry was subsequently standardised (Zieliński et al. 2019; Zielinski et al. 2020) using Gaia Synthetic Photometric (SP) magnitudes (Gaia Collaboration 2023a).

2.3. Swift observations

The Neil Gehrels Swift Observatory (Roming et al. 2005) is a multi-wavelength space telescope designed for rapid-response observations of transient phenomena. In addition to its X-ray capabilities, Swift's Ultraviolet/Optical Telescope (UVOT) provides sensitive imaging in the near-ultraviolet and optical bands. The UV coverage enabled the investigation of potential chromatic effects, blending contributions, or signatures associated with the source or lens that may be challenging to detect at longer wavelengths.

We triggered Swift through its Target-of-Opportunity programme and obtained observations for eighteen epochs with both the UVOT and X-ray Telescope (XRT), operating in the photon-counting mode. The UVOT light curves were extracted using a 5″ aperture and a 20″ background region. The data were reduced using the HEASOFT v6.36 software package and the `uvotsource` tool (Nasa High Energy Astrophysics Science Archive Research Center (HEASARC) 2014), and the resulting photometry was subsequently uploaded to BHTOM. The Swift/XRT observations were processed using the standard XRTPIPELINE procedures. No X-ray source was detected in any epoch. The XRT and UVOT coverage spans times before, during, and after the main magnification region, including several high-magnification observations.

2.4. TESS observations

The Transiting Exoplanet Survey Satellite (Ricker et al. 2015) is a space-based mission designed to perform high-precision, uninterrupted photometry over wide fields for transiting exoplanets. Unlike ground-based surveys, TESS provides nearly continuous monitoring over ∼27-day sectors with minimal gaps and without the limitations imposed by weather, seeing, or diurnal cycles. Although it is optimised for exoplanet detection, TESS has proven valuable for time-domain astrophysics more broadly, offering high-cadence light curves that are sensitive to transient events such as microlensing.

TESS observed the source (TIC 123793270) in 2018, 2020, and 2024 during Sectors 06, 33, and 87, respectively. Full-frame image (FFI) photometry was obtained with cadences of 30 minutes (Sector 06), 10 minutes (Sector 33), and 200 seconds (Sector 87). The TESS light curve covers a baseline period in 2018/2019, a period during the primary magnification region (from December 2020 until January 2021), and a period when the event had returned to its baseline magnitude (December 2024). The ≤30-minute cadence of the TESS data, most notably in Sector 33 around the peak and caustic approach, provides powerful constraints on the binary geometry.

Owing to its survey strategy and sky coverage, TESS is not well suited to detecting classical microlensing events and such events falling within the TESS footprint are expected to be rare (Sajadian et al. 2025; Yang et al. 2024). This event represents one of the first published cases in which TESS photometry was used as part of the light-curve analysis of a gravitational microlensing event. Although Kunimoto et al. (2025) proposed a free-floating planet candidate based on a single brightening event in a TESS light curve, subsequent analysis by Mróz (2024) demonstrated that this signal is more consistent with a stellar flare than with microlensing.

2.5. NEOWISE observations

The NEOWISE reactivation mission (Mainzer et al. 2011) was the extended phase of the Wide-field Infrared Survey Explorer (WISE; Wright et al. 2010), which provided time series of mid-infrared imaging of the sky in the W1 (3.4 μm) and W2 (4.6 μm) bands. Primarily aimed at identifying and characterising near-Earth objects, NEOWISE delivered valuable time-domain data; for microlensing studies, this offers the opportunity to probe the mid-infrared properties of the source and lens. At mid-infrared wavelengths, contributions from cool or dusty objects may be more readily detected than at optical or UV wavelengths. NEOWISE observations of the source span from March 2014 until February 2024. The source was routinely observed with a six-month cadence such that 21 NEOWISE-observing periods are available, of which four periods are during the time where the source was magnified.

3. Spectroscopic observations

3.1. Observing data

In addition to intensive photometric monitoring, Gaia20fnr was also observed spectroscopically by several instruments. We initiated spectroscopic follow-up with the Spectrograph for the Rapid Acquisition of Transients (SPRAT, Piascik et al. 2014) mounted on the 2-m Liverpool Telescope (LT, Steele et al. 2004) in La Palma, Canary Islands, Spain. The low-resolution spectrum (R∼350) was obtained on 23 December 2020 (HJD = 2459206.5)

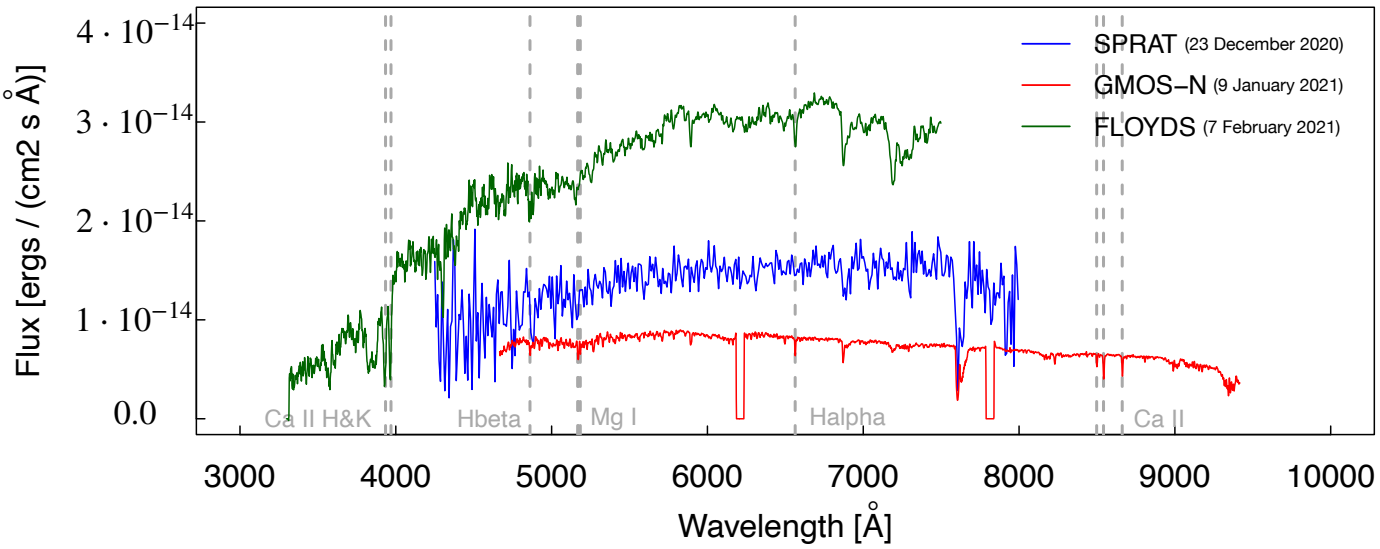


Fig. 3. Low-resolution spectra of the Gaia20fnr event observed by the SPRAT, GMOS-N and FLOYDS instruments. Vertical dashed lines present two Balmer lines, Mg I, and Ca II.

under proposal OL20B01 (PI: P. Zieliński) and covers the wavelength range 400–800 nm. The standard reduction procedure was applied by using an automated pipeline developed by the LT Team. The Xe arc lamp was used for wavelength calibration.

We also collected a low-resolution spectrum using Gemini Multi-Object Spectrographs (GMOS; Hook et al. 2004) mounted on the 8-m Gemini North Telescope (Hawaii, USA). The spectrum was obtained using the long-slit mode with the R400 grating, which provides a resolving power of R∼2000 and covers the wavelength range 400–900 nm. The observations were obtained on 9 January 2021 (HJD = 2459223.5) under proposal GN-2020B-Q-318 (PI: I. Gezer). The spectrum was bias- and flat-field corrected as well as wavelength and flux calibrated by using IRAF[4] tasks and scripts.

The third low-resolution spectrum (R∼500) was obtained with the FLOYDS spectrograph on the LCO 2-m telescope at Siding Spring Observatory, Australia (Brown et al. 2013). FLOYDS covers wavelengths from roughly 320–1000 nm. A 1.2″ slit was used for these observations. The spectrum was obtained on 7 February 2021 (HJD = 2459253.5) under proposal KEY2020B-003 (PI: E. Bachelet). All reductions were carried out using the standard LCO FLOYDS pipeline where a set of HgAr and Zn lamps are used for wavelength calibration. Due to strong fringing at the red end of the detector, we restricted our analysis to wavelengths shorter than 750 nm.

Although the three low-resolution spectra shown in Fig. 3 differ in terms of their overall appearance because of their different spectral resolutions, calibration procedures, and observing conditions, they all consistently show the features of an ordinary late-type giant star. In particular, the spectra are dominated by strong metallic and Balmer absorption lines and do not display any emission features, indicating no evidence for stellar activity, circumstellar material, or other signatures typically associated with eruptive transients. Thus, the spectroscopy supports the interpretation of Gaia20fnr as a candidate microlensing event (Zielinski et al. 2021).

For the high-dispersion spectra, we used the 10-m Southern African Large Telescope (SALT, Buckley et al. 2006). The observations were carried out on 6 February 2021 (HJD = 2459250.5) and 4 September 2021 (HJD = 2459461.5) under proposal 2018-2-LSP-001 (PI: D. Buckley). To obtain an échelle spectrum covering both the blue and red channels (3700–8800 Å), we used the High-Resolution Spectrograph (HRS; Crause et al. 2014) in its medium-resolution configuration. This setup yielded resolving powers of R ∼ 15 000 and R ∼ 17 000 for the first and second spectra, respectively. The raw data were processed with the SALT MIDAS reduction pipeline (Kniazev et al. 2016, 2017), including bias subtraction, flat-field correction, and wavelength calibration using a ThAr arc lamp. The spectra were then extracted into a one-dimensional (1D) format, order-merged, corrected for sky emission, and shifted to the heliocentric frame. We further refined the data by removing cosmic-ray hits and other artificial artefacts. Because the spectra exhibited low quality at the blue end, regions with $\lambda < 4000$Å (first spectrum) and $\lambda < 5480$ Å (second spectrum) were excluded. After these adjustments, the final spectra had an average signal-to-noise ratio (S/N) of about 90.

We also obtained observations with the X-shooter instrument (Vernet et al. 2011) on the ESO Very Large Telescope (VLT). X-shooter is a multi-wavelength medium-resolution spectrograph equipped with three independent arms, enabling simultaneous coverage of the UVB (300–559 nm), VIS (559–1024 nm), and NIR (1024–2480 nm) spectral ranges. Because each arm uses its own cross-dispersing optics, detector shutter, and slit mask, the spectral resolution differs between them. Using slit widths of 1.0″, 0.7″, and 0.6″, we achieved a resolution of $R \sim 10\,000$ and S/N∼ 750. X-shooter observations were carried out on 2 October 2021 (HJD = 2459489.5) under proposal 108.22JZ.001 (PI: L. Wyrzykowski). The data were processed with the EsoReflex pipeline[5]. Wavelength calibration was performed with ThAr lamps for the UVB and VIS arms and a combination of Ar, Hg, Ne, and Xe lamps for the NIR. A selection of the calibrated SALT/HRS and X-shooter spectra are shown in Figs. 4 and 5.

[4] https://iraf.noirlab.edu/

[5] https://www.eso.org/sci/software/esoreflex/

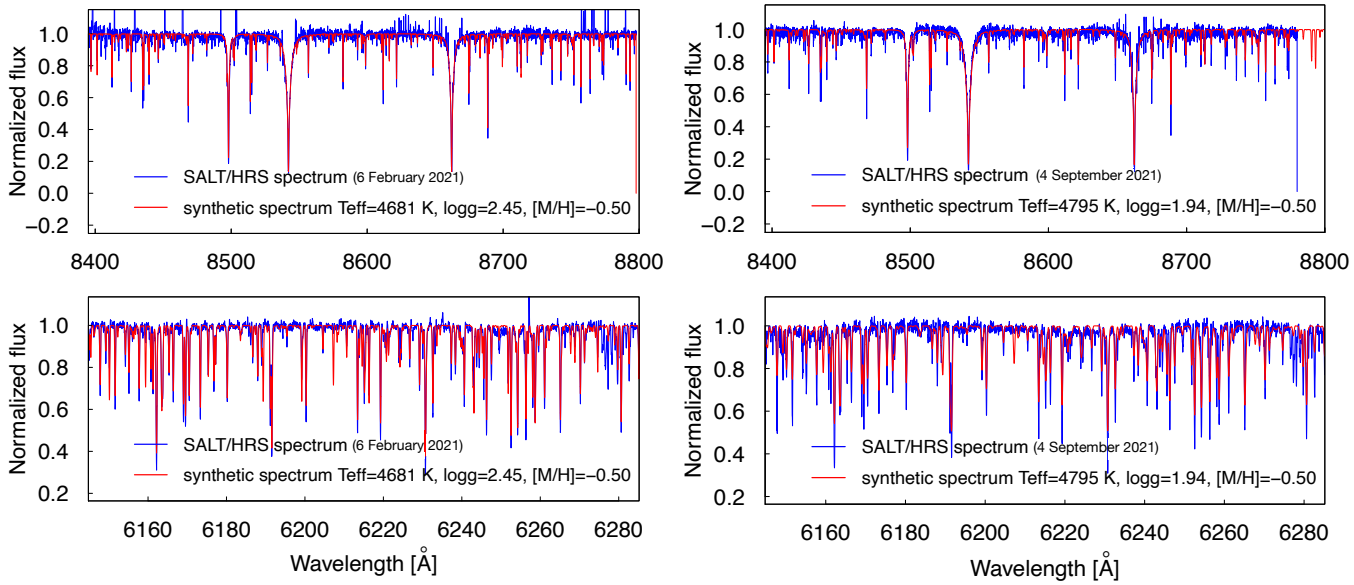


Fig. 4. Spectrum of the Gaia20fnr event (blue) observed by the SALT HRS spectrograph on 6 February 2021 (left) and 4 September 2021 (right). Shown in red is the synthetic spectrum calculated for the best-fit atmospheric parameters.

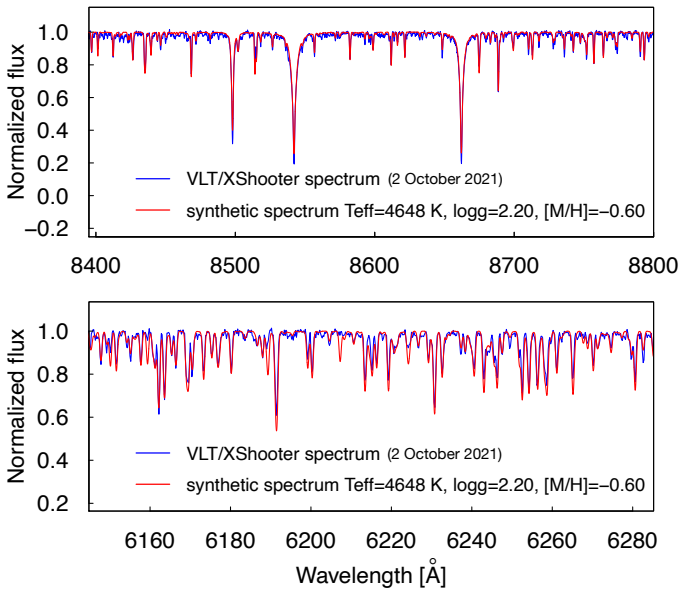


Fig. 5. Spectrum of the Gaia20fnr event (blue) observed by the X-Shooter instrument on the VLT on 2 October 2021. Shown in red is the synthetic spectrum calculated for the best-fit atmospheric parameters.

3.2. Spectral analysis

Based on three high-resolution datasets, we analysed the absorption features in Gaia20fnr. The spectral resolution of these datasets is sufficient for determining the atmospheric parameters through the `iSpec`[6] package, which incorporates several known radiative-transfer tools (Blanco-Cuaresma et al. 2014; Blanco-Cuaresma 2019). For this work, we employed the SPECTRUM code to derive the effective temperature, $T_{\rm eff}$, surface gravity, $\log g$, metallicity, [M/H], and microturbulent velocity, $v_{\rm t}$.

To generate synthetic spectra and compare them with the observations, we selected a list of atomic features including H_α, H_β, and lines of Ca, Mg, Na, Ti, and Fe, using MARCS atmospheric models (Gustafsson et al. 2008) together with solar abundances from Grevesse et al. (2007). Since nearly all measurable lines with reliable laboratory data (wavelengths, excitation potentials, oscillator strengths, etc.) appear in the VIS arm of the X-Shooter spectrum, our analysis focuses exclusively on that wavelength range.

[6] https://www.blancocuaresma.com/s/iSpec

Table 2. Stellar parameters from spectral fitting.

Parameter	SALT/HRS 1	SALT/HRS 2	X-shooter
$T_{\rm eff}$ (K)	4681 ± 265	4795 ± 79	4648 ± 353
$\log g$ (cgs)	2.45 ± 0.48	1.94 ± 0.16	2.20 ± 0.40
(M/H) (dex)	−0.50 ± 0.30	−0.50 ± 0.10	−0.60 ± 0.28
$v_{\rm t}$ (km s^{-1})	1.25 ± 0.59	1.96 ± 0.21	2.49 ± 1.08

Notes. SALT/HRS 1, SALT/HRS 2, and X-shooter correspond to the spectra obtained on 6 February 2021, 4 September 2021, and 2 October 2021, respectively.

The best-fitting synthetic spectra corresponding to the derived parameters are listed in Table 2. Figures 4 and 5 present the SALT/HRS and X-shooter data and their synthetic counterparts around the Ca II triplet, and the 6140–6280 Å region containing many Fe lines. Some parts of SALT spectra show emission-like features as, for instance, the spectrum from 6 February 2021. This is due to relatively higher noise in these parts of the spectrum and/or imperfect removal of instrumental artefacts during the calibration process. These artefacts are not intrinsic to the stellar spectrum and were not included in the fitting procedure. Across all observations, the derived parameters are consistent within uncertainties. As seen in Table 2, the most precise parameter determination was obtained for the HRS spectrum obtained on 4 September 2021, while Fig. 4 (right panels) shows the biggest discrepancy between the observed and synthetic spectra compared to the other fits. Relatively small formal uncertainties arise from the high S/N and the highest resolving power of that observation and therefore primarily reflect statistical errors, rather than the systematic discrepancies visible in

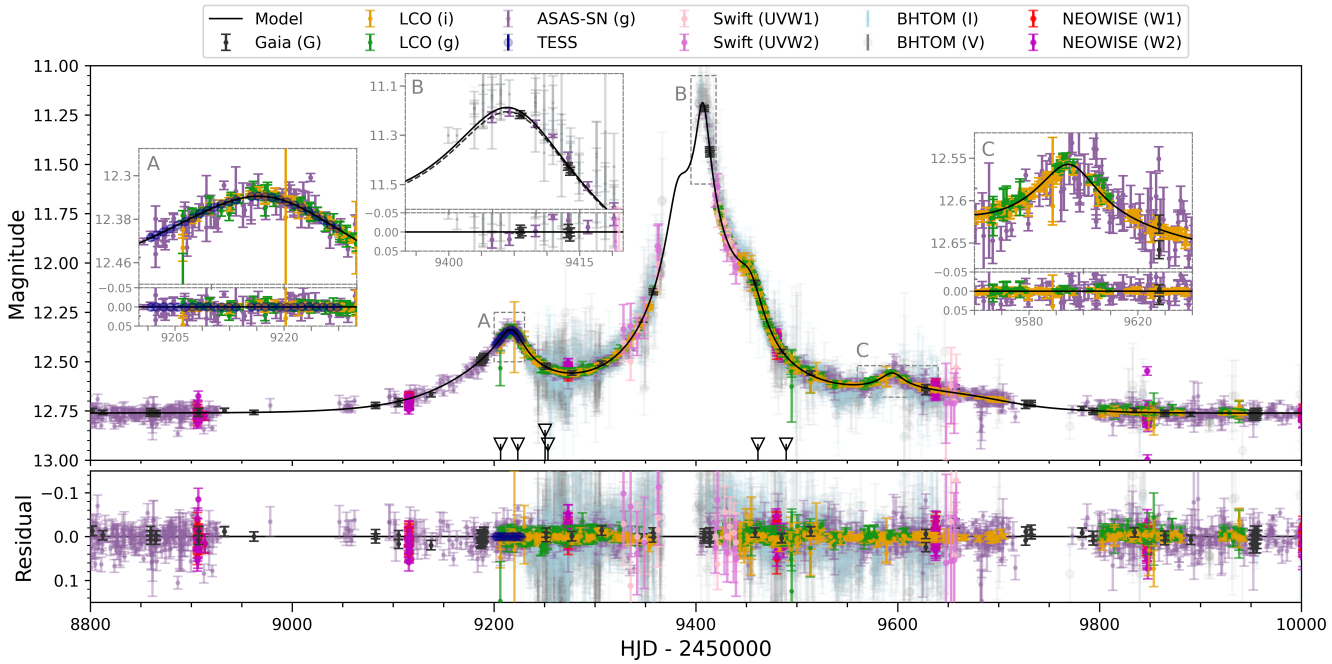


Fig. 6. Light curve of the microlensing event Gaia20fnr. Only the data used in the modelling process are shown and all measurements are transformed into the i-band magnitude scale. Data from different observatories, telescopes, and instruments are plotted together for the LCO, ASAS-SN, and BHTOM data. TESS data are binned into 24-hour bins for visibility reasons. In panel B, the space-parallax effect for Gaia is visible in the dashed line. In panel C, the BHTOM data are left out for visibility reasons. The inverted triangles along the x-axis indicate the epochs at which the spectra were obtained.

the fit. Based on the results, we classified the source star of the Gaia20fnr microlensing event as a metal-deficient K2-type giant. Furthermore, none of the high-resolution spectra show any absorption features of a secondary component.

4. Microlensing model

4.1. Data preparation

Due to the complexity of the microlensing event, the data used for modelling were restricted to the data shown in Fig. 6. By selecting data from instruments that observed for substantial parts of the light curve, specifically regions during the magnification as well as at baseline, the efficiency of the fitting procedure was dramatically increased. We emphasise that unmagnified data points do not impose constraints on the microlensing model parameters because the microlensing solution is determined through a non-linear fit.

Gaia (G-band) and ASAS-SN (g-band) data cover the entire magnification region as well as a substantial time during the baseline before and after the microlensing event, starting from before 2015 and 2018, respectively. The LCO observations in the g and i bands, together with the BHTOM observations in the i, B, V, and I bands provide good temporal coverage during the source magnification phase and after the microlensing event had returned to baseline.

For the modelling, high-cadence and high-precision LCO datasets were vital in achieving model convergence. After removing instrumental signatures with the BANZAI pipeline (McCully et al. 2018), the time-series photometry was derived with the pyDANDIA software package (Bramich 2008; Bramich et al. 2013) and extracted to the reference frames (Street et al. 2024a). Conventionally, the Sinistro instruments from different LCO observing sites can then be modelled as one single instrument; however due to the extensive data from the Cerro Tololo Inter-American Observatory, the South African Astronomical Observatory, and the Siding Spring Observatory, we choose to model them as individual telescopes/instruments with independent source-blend flux ratios.

To speed up the initial modelling processes, data were binned into 24-hour segments. Considering that there were no caustic crossings in this event, the binning was conservative and could have been with larger bins to speed up the initial modelling process. For the final models, data were unbinned and each instrument flux was modelled individually. The error bars of each dataset were rescaled according to common microlensing practice (Skowron et al. 2011; Yee et al. 2012; Miyake et al. 2012), such that

$$\sigma_i = k\sqrt{\sigma^2_{i,\mathrm{orig}} + e^2_{\mathrm{min}}}, \tag{1}$$

where $\sigma_{i,orig}$ is the original data error, and e^2_{min} and k are such that $\chi^2/\mathrm{dof} \approx 1$ and the cumulative sum of χ^2 is approximately linear as a function of source magnification. The coefficients e^2_{min} and k are determined independently for each dataset and the data were cut such that data with an error greater than three times the median were excluded.

4.2. Binary lens model

We adopted the standard gravitational microlensing formalism, where a foreground lens deflects the light of a background source and produces a time-varying magnification as the projected relative lens–source position changes. The characteristic angular

scale of the problem is the angular Einstein radius,

$$\theta_{\rm E} = \sqrt{\frac{4\,G\,M_{\rm L}}{c^2}\,\frac{D_{\rm S}-D_{\rm L}}{D_{\rm S}\,D_{\rm L}}}, \tag{2}$$

where $M_{\rm L}$ is the total lens mass and $D_{\rm L}$ and $D_{\rm S}$ are the lens and source distances, respectively.

As a reference, we begin with the Paczyński point-source point-lens (PSPL) model (Paczynski 1986), defined by the parameters $\{t_0,\, u_0,\, t_{\rm E}\}$, where t_0 is the epoch of closest approach, u_0 is the minimum impact parameter in units of $\theta_{\rm E}$, and $t_{\rm E}$ is the Einstein timescale. The PSPL model can be extended to include higher order effects such as the angular source radius in Einstein units ($\rho = \theta_\star/\theta_{\rm E}$) and the microlens parallax ($\pi_{\rm E} = \sqrt{\pi^2_{\rm E,N} + \pi^2_{\rm E,E}}$). It provides a useful baseline to approximate t_0 but cannot reproduce the pronounced anomalies associated with the multi-peaked structure observed in the light curve.

The PSPL model is extended to the point-source binary-lens (PSBL) model following the standard parametrisation used throughout the microlensing literature (Gaudi 2012). The binary lens extends the model by: (i) the projected separation, s, between the two lens components in units of $\theta_{\rm E}$; (ii) the mass ratio, $q = M_2/M_1$, of the binary lens; (iii) the angle, α, between the source trajectory and the binary-lens axis.

The topology of the caustic curves of a binary lens depends primarily on (s, q), and the close ($s \ll 1$), resonant ($s \simeq 1$), and wide ($s \gg 1$) regimes are all in principle allowed (Erdl & Schneider 1993; Dominik 1999). Viable solutions commonly appear in close–wide pairs owing to the $s \leftrightarrow 1/s$ degeneracy.

Because the magnification $A(t)$ of a source due to gravitational microlensing is achromatic, the model flux in each dataset i that describes a telescope and filter is written as

$$F_i(t) = A(t)\,F_{{\rm s},i} + F_{{\rm b},i}, \tag{3}$$

where $F_{{\rm s},i}$ and $F_{{\rm b},i}$ are the dataset-dependent source and blend flux, respectively. The geometric microlensing parameters are shared across all datasets, while the flux parameters are independent. The blend flux parameters contain contributions from the lens, an unrelated object in the line of sight, or both. This can provide constraints on the lens brightness and colour, which can reveal additional information about the nature of the lens. Given the long timescale of the event, magnified at $A > 1.05$ for more than 500 days, and its multi-platform coverage, higher order effects are also considered.

4.3. Higher order effects

4.3.1. Annual and satellite microlensing parallax

Annual parallax arises from Earth's orbital motion and is represented in the geocentric frame by the vector $\boldsymbol{\pi}_{\rm E} = (\pi_{\rm E,N}, \pi_{\rm E,E})$, such that

$$\pi_{\rm E} = \frac{\pi_{\rm rel}}{\theta_{\rm E}} \qquad \text{and} \qquad \pi_{\rm rel} = {\rm AU}\left(\frac{1}{D_{\rm L}} - \frac{1}{D_{\rm S}}\right), \tag{4}$$

following Gould (2004). The microlens parallax introduces long-term distortions in the light curve, especially in the wings.

Space-based microlensing parallax, first proposed in Refsdal (1966), is obtained by observing the same microlensing event simultaneously from Earth and a satellite (Gould 1994). It has since proven to be observable and able to measure the microlensing parallax vector, from which the lens mass and distance are determined (e.g. Dong et al. 2007; Udalski et al. 2015; Yee et al. 2015). Space-parallax signatures are particularly evident in data from space telescopes such as Spitzer (Werner et al. 2004), whose large Earth–spacecraft separation yields a strong parallax baseline. Nonetheless, they have also been measured in Gaia microlensing events (e.g. Wyrzykowski et al. 2020; Kruszyńska et al. 2022).

As the Gaia20fnr microlensing event was observed by four space telescopes, the ephemeris of each space telescope is considered in the light curve modelling. As the NEOWISE and Swift space telescopes are in low-Earth orbit this effect is not observable for this event with these telescopes. The TESS space telescope is in a highly-elliptical, high-altitude orbit, such that space-parallax is in theory observable; however it is not observed for this event. The Gaia spacecraft, observing at Lagrange-Point L2, is most sensitive to the satellite parallax, and shows a space-parallax signal. This space-parallax is only observable at the closest approach of the source and the lens and it has an insignificant effect on the light curve and model parameters.

4.3.2. No finite-source effects

Finite source effects become detectable when the magnification gradient across the source star is large enough to be resolved in the light curve. This typically occurs during caustic crossings, where the magnification varies strongly over small angular scales (Yoo et al. 2004; Zub et al. 2011). Although extracting these signals is more difficult in non-caustic-crossing binary events, finite-source signatures may also be recovered because the magnification pattern expands around cusp regions (Dominik 1999; Gaudi & Gould 1999).

When finite-source effects are measurable, the combination of limb-darkened light-curve modelling and an independently estimated angular source radius $\theta_\star$ yields a direct estimate of the angular Einstein radius, $\theta_{\rm E} = \frac{\theta_\star}{\rho}$. In our finite-source binary-lens (FSBL) modelling, we include the finite angular size of the source star following the formalism of Albrow et al. (1999) with linear limb darkening implemented as described by Bachelet et al. (2012). For this event, the light curve does not show evidence of finite-source effects: models including ρ fit the data no better than point-source models and ρ fails to converge.

4.3.3. Keplerian orbital motion

Binary-lens microlensing events may deviate from the static-lens approximation if the projected separation or orientation of the lens components changes appreciably during the event. For sufficiently long timescales, orbital motion must be taken into account to avoid systematic biases in the inferred lens parameters (Dominik 1999; Albrow et al. 2000). As a first step, we include linear orbital motion by allowing the projected separation s and the position angle α of the binary axis to vary with constant time derivatives, ds/dt and $d\alpha/dt$. This formalism provides a first-order description of orbital effects when only a small fraction of the orbit is covered.

For Gaia20fnr, the event duration represents a non-negligible fraction of the expected orbital period of the binary lens. In this regime, a full Keplerian treatment is required. We therefore adopt the parameterisation by Skowron et al. (2011), which was adapted by Bozza et al. (2021), in which the lens system is described by its three-dimensional (3D) position and velocity at a chosen reference epoch in the lens centre-of-mass frame. The subsequent evolution of the system is obtained by integrating the

Newtonian two-body problem, ensuring that all trial solutions correspond to dynamically consistent orbits.

The six-dimensional (6D) phase-space vector at the reference epoch can be transformed into the standard set of orbital elements of the binary: the semi-major axis, a, orbital period, P, eccentricity, e, inclination, i, longitude of the ascending node, Ω, argument of periapsis, ω, and time of periastron passage, $t_{\rm peri}$. These elements uniquely define the 3D orbit and, in particular, the projected positions of the two components on the sky as a function of time. In earlier binary microlensing events with measurable orbital motion, a Keplerian model typically provided only a modest improvement over the linear approximation (Skowron et al. 2011; Shin et al. 2012), because the observed light curves covered only a limited portion of the orbit. In contrast, for Gaia20fnr the similarity between the orbital period and the event timescale, together with the clear detection of repeated light-curve features, means that the Keplerian description yields a significantly better fit than both the static and linear-orbit models and is therefore required for a physically reliable interpretation of the event (Penny et al. 2011a).

We find that an additional degenerate configuration exists in our microlensing model, which differs only by a simultaneous sign reversal of $r_{\rm s}$ and $\gamma_{\rm radial}$, i.e. $(r_{\rm s}, \gamma_{\rm radial}) \rightarrow (-r_{\rm s}, -\gamma_{\rm radial})$. This alternative solution yields the same physical parameters, except that Ω and ω transform as $\Omega \rightarrow \pi - \Omega$ and $\omega \rightarrow \omega - \pi$, respectively, and the sign of the radial velocity is reversed.

4.4. Modelling methods and degeneracies

Higher order effects in the PSBL model can be explored both individually and in combination to assess potential degeneracies inherent to photometric microlensing data. In this work, the modelling was carried out with the `pyLIMA` software package (Bachelet et al. 2017), which provides a flexible, modular framework for microlensing analysis and offers interfaces to fast binary-lens magnification solvers. In particular, `pyLIMA` employs the `VBMicrolensing` backend (Bozza et al. 2021; Bozza et al. 2025), which implements an advanced contour-integration algorithm for accurate computation of finite-source binary-lens magnifications. `pyLIMA` has been successfully used to model a variety of microlensing events (e.g. Bachelet et al. 2024b, 2018).

The binary-lens parameter space is high-dimensional and can contain multiple local minima associated with known degeneracies. To explore these minima robustly, we initially adopted a strategy for a global search using a differential evolution (DE) algorithm, which is a population-based stochastic optimisation method (Storn & Price 1997) that is well suited to multi-modal problems. We initialised the DE population across wide ranges in all fit parameters. The `pyLIMA` algorithms evaluate the log-likelihood across all datasets, solving analytically for $(F_{{\rm s},i}, F_{{\rm b},i})$ for speed. After convergence, we identify the families of solutions (e.g. close vs wide, positive vs negative u_0) and retained all models within a small $\Delta\chi^2$ of the best minimum to seed the Markov chain Monte Carlo (MCMC) stage. We then explore the posterior distribution around each DE minimum with MCMC as implemented in `pyLIMA` via `emcee` (Foreman-Mackey et al. 2013).

4.5. Best-fit model results

The best-fit result for the close ($s < 1$) binary-lens model is shown in Table 3. The MCMC chains only converged for the PSBL model that considered parallax and full Keplerian orbital motion. The source and blend magnitudes for the best model, shown in Table 4, predict a flux ratio,

$$\left(\frac{f_{\rm source}}{f_{\rm source} + f_{\rm blend}}\right) \simeq 0.98; \quad \left(\frac{f_{\rm blend}}{f_{\rm source}}\right) \simeq 0.02$$

in the optical bands. NEOWISE observations determine a flux ratio of 0.985 and 0.970 in the W1 and W2 bands, respectively. Swift optical bands are in agreement with other optical observations such as Gaia and LCO; however, the UV bands have a flux ratio ~1.0, indicating that there is no significant UV light observed from the blending object. The light curve and best-fitting model, showing the unique, non-caustic-crossing structure, are presented in Fig. 6. The geometry of the event and the motion of the source projected into the lens plane is shown in Fig. 7.

The modelling approach outlined above provided no solution with a wide ($s > 1$) geometry. Similarly, binary source models with xallarap cannot reproduce the observed light curve.

Table 3. Best-fit PSBL microlensing parameters.

Parameter	PSBL model
t_0 (JD-2450000)	$9403.881^{+0.095}_{-0.098}$
u_0	$-0.255^{+0.002}_{-0.002}$
$t_{\rm E}$ (days]	$69.418^{+0.403}_{-0.401}$
s	$0.492^{+0.003}_{-0.003}$
q	$1.134^{+0.016}_{-0.017}$
α	$4.496^{+0.005}_{-0.005}$
$\pi_{\rm E,N}$	$-0.185^{+0.001}_{-0.001}$
$\pi_{\rm E,E}$	$0.395^{+0.003}_{-0.003}$
$\gamma_{\parallel}$	$1.577^{+0.047}_{-0.050}$
$\gamma_{\perp}$	$-2.640^{+0.060}_{-0.061}$
$\gamma_{\rm radial}$	$-4.704^{+0.022}_{-0.020}$
$r_{\rm s}$	$0.378^{+0.015}_{-0.016}$
$a_{\rm s}$	$0.982^{+0.002}_{-0.002}$
χ^2/d.o.f.	2246.9/2247.0

Notes. Values and uncertainties correspond to the 16th, 50th, and 84th percentiles of the MCMC chains.

Table 4. Source and blend magnitudes.

Filter	Source	Blend
G	$13.18^{+0.01}_{-0.01}\left(^{+0.03}_{-0.03}\right)$	$17.63^{+1.00}_{-0.50}\left(^{+9.77}_{-1.16}\right)$
g	$13.90^{+0.01}_{-0.01}\left(^{+0.03}_{-0.03}\right)$	$17.78^{+0.43}_{-0.31}\left(^{+2.21}_{-0.74}\right)$
i	$12.80^{+0.01}_{-0.01}\left(^{+0.03}_{-0.03}\right)$	$16.63^{+0.40}_{-0.29}\left(^{+2.83}_{-0.77}\right)$

Notes. Values and uncertainties correspond to the 16th, 50th, and 84th percentiles. Values in parentheses give the 3 interval, corresponding to the 0.135th and 99.865th percentiles.

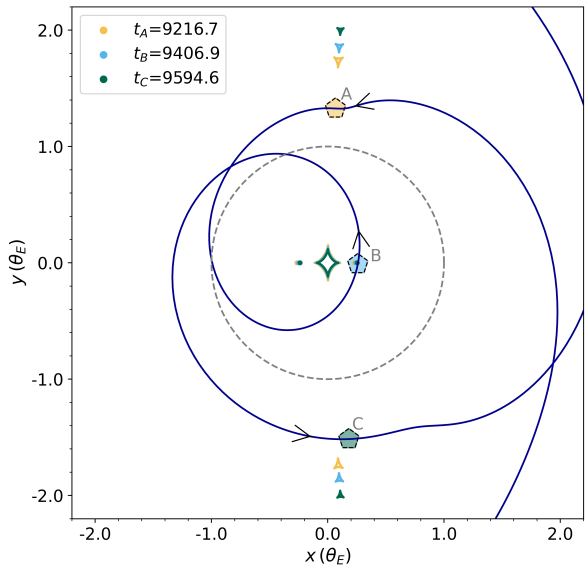


Fig. 7. Source trajectory and caustic geometry of the best-fit model shown for three timestamps. The dark blue line represents the source motion in the lens plane, strongly characterised by the parallax and orbital motion signals. The filled circles at $y(\theta_E) = 0.0$ represent the lens positions. The outlined shapes mark the caustic structures. The different structures arise as a consequence of the orbital motion of the lens. The shaded pentagon markers represent the positions of the source in the lens plane at the three timestamps.

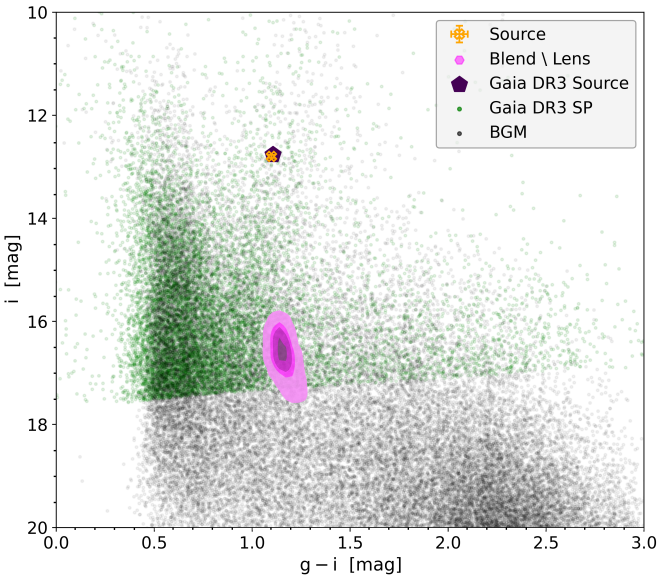


Fig. 8. Colour-magnitude diagram. Black dots are Besançon Galaxy Model (BGM) neighbours within 1 degree of the source (Robin et al. 2003; Czekaj et al. 2014). Green dots are the Gaia DR3 Synthetic Photometry Catalogue neighbours within 1 degree of the source (Gaia Collaboration 2023a). The purple pentagon is the Gaia DR3 source of the Gaia20fnr GSA alert (Gaia Collaboration 2023b). The orange x-shaped marker shows the source position for the best model photometry. The pink contours indicate the blend position corresponding to the best-fitting photometric model, with contour levels enclosing the 20th, 40th, 60th, and 80th percentiles of the MCMC posterior.

5. Physical parameters

5.1. Gaia DR3 parameters

The alert of the microlensing event occurred on 2 December 2020 and our best model predicts that a magnification $A > 1.05$ did not occur before September 2020. The lens-source separation did not cross the unit Einstein radius ($u = 1$) until December 2020. Gaia DR3 is based on data obtained until mid-2017, with the last observations for ID 2990431491637998848 made on 2 May 2017. Although the final observations used for the five-parameter solutions published in Gaia DR3 were more than three years before the start of the photometric microlensing event, one cannot rule out that the astrometric microlensing signal influenced the source parameters published in Gaia DR3 (e.g. Rybicki et al. 2018; Kruszyńska et al. 2022; Maskoliūnas et al. 2024). Additionally, the best model results with non-zero blend flux mean that Gaia flux measurements come from the combined flux of the source and the blend. This could be another potential contaminant to Gaia DR3 5-parameter solutions. Thus, even for microlensing events that begin well outside the Gaia DR3 timeframe, it is essential to scrutinise the Gaia DR3 source parameters before using them in further analysis.

The flux ratio determined in the Gaia G band is such that the flux-weighted parallax, determined as the combined signal of source and blend parallax (Rota et al. 2024), does not deviate significantly from the value published in Gaia DR3. The colour-magnitude diagram (CMD), in Fig. 8, shows that the best-model source flux in SDSS bands is in good agreement with the Gaia DR3 Synthetic Photometry Catalogue (GSPC; Gaia Collaboration 2023a) values of the source. In the CMD, the source lies in or near the RC region, consistent with the 12.16 $R_\odot$ radius inferred from TESS and with the K-type giant parameters reported in Gaia DR3. A RUWE of 1.03 and a significant, positive, and non-zero parallax, $\varpi = 0.2875 \pm 0.0125$ mas, imply a robust astrometric solution. We therefore assume that the values published in Gaia DR3 are consistent with measurements of the source of the microlensing event.

5.2. Source distance, extinction, and type

To determine the physical properties of the lensing event (Eq. (2)), a distance estimate for the source star (D_S) is essential. The source star distance published for the Gaia DR3 source is determined from the parallax as $D_s = 3099 \pm 109$ pc. The Bailer-Jones et al. (2021) catalogue distances, which were calculated based on Gaia parallaxes and photometric measurements, are in agreement with this value. The geometric distance, based on the parallax and its uncertainties, gives the distance to the source star 3016^{+130}_{-123} pc. The photo-geometric distance is determined by the parallax, the colour, and the observed magnitude of the star, and gives a distance 3109^{+97}_{-113} pc. For the following calculations the source distance from the Bailer-Jones et al. (2021) catalogue, 3109^{+97}_{-113} pc, is used. This corresponds to an angular source radius of $\theta_\star = R_S/D_S \approx 18$ µas.

Given the significant extinction towards Galactic bulge microlensing fields, red clump (RC) giants in the CMD serve as standard candles for estimating the interstellar extinction along the line of sight (Yoo et al. 2004; Nataf et al. 2013; Bensby et al. 2013). In regions as isolated as the Gaia20fnr event, no statistically significant RC population, located along the red giant branch of the CMD, can be clearly separated from the main sequence. We therefore use the excess colour between the modelled source fluxes and the intrinsic colour estimated from the spectroscopic classification of the source to constrain the extinction in the line of sight of the microlensing event. The event lies

at a relatively high Galactic latitude where the dust column density, and thus the extinction, is markedly lower than towards the bulge microlensing fields. Even so, the extinction is not negligible and must be included when determining the intrinsic source and blend colours and luminosities.

To estimate the intrinsic source colour, we used the three spectroscopic solutions listed in Table 2. For each set of atmospheric parameters ($T_{\rm eff}$, $\log g$, [M/H]), we interpolated the Houdashelt et al. (2000) grid to obtain the corresponding intrinsic colour $(V-I)_0$. We then adopted the mean of the three resulting $(V-I)_0$ values as the intrinsic colour of the source, while the quoted uncertainty includes the scatter among the three estimates. This yields $(V-I)_0 = 1.016 \pm 0.010$ mag. Using the colour–colour relations from Jordi et al. (2006), the intrinsic K2-type giant colour can be converted to an intrinsic SDSS colour of $(g-i)_0 = 0.974 \pm 0.010$ mag.

The source magnitudes in the g and i bands are constrained to within 0.01 mag using data from the 1-m Sinistro telescopes of LCO at Siding Spring Observatory. From these measurements, the excess colour is estimated as $E(g-i) = (g-i)_{\rm observed} - (g-i)_{\rm intrinsic} = 0.125^{+0.015}_{-0.015}$. This corresponds to an extinction of $A_{\rm g} = 0.2570^{+0.019}_{-0.019}$ mag and $A_{\rm i} = 0.1321^{+0.010}_{-0.010}$ mag. Applying these values to the LCO observations from Siding Spring yields corrected source magnitudes of $m_{\rm g,LCO-SS} = 13.64^{+0.02}_{-0.02}$ mag and $m_{\rm i,LCO-SS} = 12.67^{+0.01}_{-0.01}$ mag.

In combination with the standard extinction coefficients for SDSS filters from a standard reddening law ($c_{\rm g} = 3.303$ and $c_{\rm i} = 1.698$) (Cardelli et al. 1989; Schlafly & Finkbeiner 2011), the relation $E(g-i)/E(B-V) = 1.605$ predicts the extinction of the source in JC bands. These approximate transformations from the SDSS to JC photometric system (Jordi et al. 2006; Schlafly & Finkbeiner 2011) predict a V-band extinction of $A_{\rm V} = 0.24 \pm 0.02$ mag, which we can compare to other sources for an independent confirmation of our derived extinction parameters.

The commonly used extinction maps of Marshall et al. (2006) do not cover regions located as far from the Galactic centre as is the case for this event. The extinction value in Schlafly & Finkbeiner (2011), derived from the colours of stars with spectra in the SDSS, is $A_{\rm V} = 0.224$ mag. The dust maps of Schlegel et al. (1998) predict $A_{\rm V} = 0.2605$ mag. The Besançon Galaxy Model (BGM) (Robin et al. 2003; Czekaj et al. 2014) is a population synthesis framework that simulates the stellar content and structural components of the Milky Way based on observational constraints for Galactic formation, evolution, and kinematics. It provides predictions of stellar distributions and observable properties along any line of sight and is widely used for interpreting survey data and modelling Galactic stellar populations in microlensing studies (e.g. Penny et al. 2013; Bachelet et al. 2022). The BGM derives extinction data from a diffuse extinction model and predicts the extinction in the direction of the microlensing event as $A_{\rm V,BGM} = 0.260^{+0.026}_{-0.024}$ for the source distance. This is in agreement with the values derived above.

Additionally, we use optical archival photometry data from the TESS catalogue (Stassun et al. 2019) to verify the extinction and distance values for the K2 giant source star. The unmagnified source star was measured with $B = 14.442 \pm 0.023$ mag and $V = 13.356 \pm 0.057$ mag. According to Straižys (1992), the intrinsic colour of the K2 giant should be $(B-V)_0 = 1.16$ mag with a typical absolute magnitude $M_{\rm V} = 0.7 \pm 0.3$ mag. For the standard reddening law in the diffuse ISM of the Milky Way, we assume $R_{\rm V} \sim 3.1$ (Cardelli et al. 1989) such that the estimated colour excess value is $E_{B-V} = 0.075 \pm 0.061$ and the extinction is $A_{\rm V} = 0.23 \pm 0.19$ mag. The photometric distance calculated with the TESS photometry is $D_{\rm S} = 3.06 \pm 0.77$ kpc, which is in agreement with the values published in Gaia DR3.

We determined the kinematic properties of the source star by integrating its orbit over 5 Gyr within a theoretical Milky Way potential, using the Python-based galactic dynamics package `galpy` (Bovy 2015). For the integration, we adopted the gravitational potential `MWPotential2014`, which combines components for the bulge, disk, and halo. Proper motions, radial velocity, and sky coordinates were taken from the Gaia catalogue, and the source distance from this work. From these data, we derived a mean galactocentric distance of $R_{\rm mean} = 13.7 \pm 0.37$ kpc, a maximum vertical height from the Galactic plane of $|z_{\rm max}| = 1.75 \pm 0.09$ kpc, and an orbital eccentricity of $e = 0.25 \pm 0.01$. Our kinematic analysis indicates that the source star is most likely a thin-to-thick disk object.

To estimate the source age and mass, we employed `UniDAM`, which uses a Bayesian approach combined with `PARSEC` isochrones (Bressan et al. 2012), stellar atmospheric parameters (derived from our spectroscopic analysis), and infrared magnitudes (Mints & Hekker 2017, 2018). The required J, H, and K magnitudes from the 2MASS Survey and the $W1$ and $W2$ magnitudes from AllWISE were provided as input to `UniDAM`. The resulting age and mass of the source star are $4.7^{+3.7}_{-1.3}$ Gyr and $1.2 \pm 0.3\ M_\odot$, respectively.

5.3. Physical parameters of the binary lens

A direct lens mass estimate based on the microlensing model is given by

$$M_{\rm L} = \frac{\theta_{\rm E}}{\kappa \pi_{\rm E}}. \tag{5}$$

As the FSBL best-fit model does not constrain the finite source effects, a direct calculation of the lens mass and distance is not possible. Instead, if an estimate of the lens distance can be made, the lens mass can be calculated as

$$M_{\rm L} = \frac{\pi_{\rm rel}}{\kappa \pi_{\rm E}^2}. \tag{6}$$

In cases where the finite source effects are not constrained, microlensing studies have often relied on Galactic models to constrain the parameters of the lens (e.g. Bachelet et al. 2022; Kruszyńska et al. 2022; Howil et al. 2025). For equal-mass binaries with $q \sim 1$, as is the case for the microlensing event in this study, these Galactic models tend to underestimate the mass of the lens due to the underlying parameter relations being calibrated on single-star populations.

DarkLensCode (DLC) (Howil et al. 2025) estimates the probability distributions of lens mass, distance, and luminosity in microlensing events from microlensing parameters and Galactic population priors. To test its effectiveness in determining lens parameters for this event, we run the analysis for model parameters excluding the blend flux. This method estimates the total lens mass as $0.98 \pm 0.38\ M_\odot$ in the 16th to 84th percentile range, which is in agreement with the values determined from our methods outlined below. At the 3σ level, DLC does not add additional constraints on the lens mass and distance beyond those imposed directly by the model parameters. It is therefore not considered further in this analysis.

We identify three avenues to constrain the lens mass. The lens mass as a function of the lens distance, constrained by these three methods, is shown in Fig. 9.

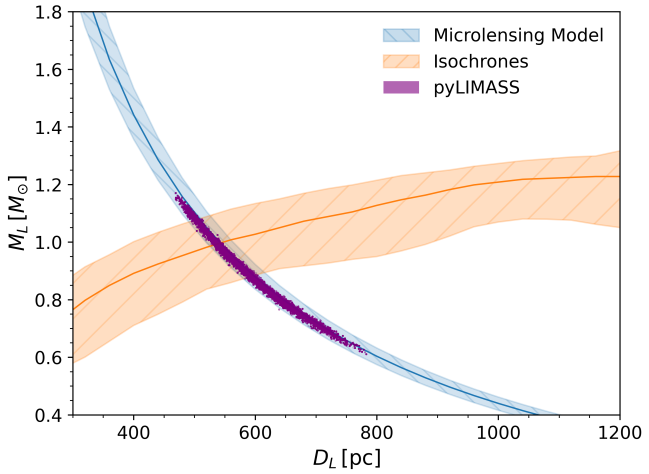


Fig. 9. Lens distance vs mass plot with distributions for our three methods of lens mass estimation. The blue region shows values determined based on constraints from the physical microlensing model. The purple distribution shows the posterior chains of the MCMC analysis with `pyLIMASS` (Bachelet et al. 2024a). The orange region shows the values determined for `PARSEC` isochrones (Nguyen et al. 2022), assuming the blend light is coming from the lens and that the isochrone limits account for the binary nature of the lens.

Firstly, the microlensing parameters in Equations (2) and (4), specifically the microlensing parallax $\pi_{\rm E}$, predict the lens mass as a function of lens distance. Secondly, `pyLIMASS` (Bachelet et al. 2024a), an algorithm that leverages information from the microlensing event with stellar isochrones in a Gaussian mixture approach, is implemented. For this event, `pyLIMASS` is able to set strong bounds on the mass-distance relation determined only by considering the constraints from the microlensing parameters. Lastly, stellar isochrones can be used to unravel the nature of the blend flux, which, assuming that the blend light is coming from the lens, can help identify the lens nature.

The blended light detected in a microlensing event could either come from the lensing objects, from neighbouring objects that are unresolved in the field of view but not magnified by the lens, or from a combination of both. Given the isolated nature of the Gaia20fnr microlensing event (see Fig. 1), the most probable case is that the lens light causes the modelled blend flux. We therefore assume that the blended light comes solely from the binary lens object and will show that this is a self-consistent assumption. As the distance to the lens is not known, we do not assume that the source and lens are equally reddened, nor do we assume that the lens suffers from no extinction. The extinction of the BGM is modelled as a function of distance using a logistic growth function and is used to deredden the blend magnitude. The CMD (Fig. 8) illustrates that the (g-i) colour of the blend is well constrained despite significant uncertainties in the magnitude presented in Table 4. It is important to note that the blend flux consists of the light from both binary objects. The distribution of blend/lens colour and magnitude is shown in the CMD (Fig. 8).

The dereddened photometric results of the blend can be leveraged with stellar isochrones from `PARSEC` (Nguyen et al. 2022), and the mass ratio determined in the microlensing model to constrain the mass of the binary lensing object. We infer the component masses and distance of an unresolved binary microlens by combining the microlensing parallax constraint with the unresolved g- and i-band fluxes interpreted through stellar isochrones at a fixed mass ratio $q = M_2/M_1$. For a set of distances, defined in the line of sight of the observer to the source, each scenario is computed. The extinction is determined as a function of distance using the parametric fit of extinction values in the BGM. The apparent magnitude of the combined binary lenses is determined as

$$M_{\rm g}^{\rm obs}(D_{\rm L}) = g_0(D_{\rm L}) - 5\log_{10}(D_{\rm L}/10\,{\rm pc}) \tag{7}$$

where $g_0 = m_{\rm g} - A_{\rm g}(D_{\rm L})$. For a stellar isochrones grid of metallicity ([Fe/H] $\in [-1.0, 0.5]$) and ages (1–12 Gyr), we build interpolators for single-star absolute magnitudes as a function of mass $M_{\rm g}$(Mass), $M_{\rm i}$(Mass). The unresolved absolute magnitudes of the binary in band $X \in \{g, i\}$ are

$$M_X({\rm Mass_{tot}}) = -2.5\log_{10}\left(10^{-0.4M_X({\rm Mass}_1)} + 10^{-0.4M_X({\rm Mass}_2)}\right). \tag{8}$$

To avoid confusion in the notation, the absolute magnitudes are marked as 'M' and the lens-component masses as 'Mass'. We were able to determine the absolute magnitude of our binary lens in the g and i bands as a function of the distance to the binary lens. By interpolation, this estimates the total mass with a fixed mass ratio, q, so that the individual masses of the binary lens could be determined.

The total lens mass is determined to be $0.97 \pm 0.12\,{\rm M}_\odot$. For the best-model mass ratio, this constrains the mass of the binary components as $M_{\rm L,1} = 0.46 \pm 0.06\,{\rm M}_\odot$ and $M_{\rm L,2} = 0.52 \pm 0.06\,{\rm M}_\odot$. The lens distance is determined to be 536 ± 45 pc. This constrains the angular Einstein radius as $\theta_{\rm E} = 3.50 \pm 0.28$ mas and the physical Einstein radius is $R_{\rm E} = 1.87 \pm 0.13$ AU. Given these results and assuming that the lensing stars are on the main sequence, we can conclude that the binary lens is consistent with late-K to early-M type stars. For the lens distance determined, the recovered extinction is $A_{\rm g,L} = 0.26 \pm 0.02$ and $A_{\rm i,L} = 0.13 \pm 0.01$, such that the extinction-corrected magnitude of the combined binary lens components is $m_{\rm g_0,L} = 17.52^{+0.43}_{-0.31}$ and $m_{i_0,{\rm L}} = 16.50^{+0.40}_{-0.29}$.

5.4. Lens and source kinematics

The precise source parameters in Gaia DR3 combined with the lens parameters determined above enable a full description of the kinematics of the lens and the source as shown in Rota et al. (2024). The photometric modelling constrains $t_{\rm E}$ in the geocentric frame, such that the geocentric relative proper motion is

$$\mu_{\rm rel,geo}({\rm N,E}) = (-7.8 \pm 0.6, 16.6 \pm 1.3)\,{\rm mas\,yr^{-1}}. \tag{9}$$

The heliocentric relative proper motion is given as

$$\boldsymbol{\mu}_{\rm rel,hel} = \frac{\theta_{\rm E}}{t_{\rm E}}\hat{\boldsymbol{\pi}}_{\rm E} + \frac{\pi_{\rm rel}}{\rm AU}\boldsymbol{v}_{\oplus,\perp}, \tag{10}$$

where $\boldsymbol{v}_{\oplus,\perp}$ is the Earth's projected velocity parallel to the lens plane, at the time t_0. It is determined from `Astropy` ephemeris (Astropy Collaboration 2013) as $\boldsymbol{v}_{\oplus,\perp}({\rm N,E})(t_0) = (5.46, -28.17)\,{\rm km\,s^{-1}}$, such that the Earth's line of sight velocity to the microlensing event is $5.9\,{\rm km\,s^{-1}}$.

The relative heliocentric proper motion is calculated to be

$$\boldsymbol{\mu}_{\rm rel,hel}({\rm N,E}) = (-6.0 \pm 0.5, -7.4 \pm 1.0)\,{\rm mas\,yr^{-1}}. \tag{11}$$

For the source proper motion (Table 1), confirmed by TESS observations of $\mu_{\rm RA} = -2.331 \pm 0.027\,{\rm mas\,yr^{-1}}$ and

Table 5. Lens orbital parameters.

Orbital parameters	
Reference time $t_{\rm ref}$	2459406.3
Orbital period P (yr)	$0.67^{+0.04}_{-0.04}$
Semi-major axis a (AU)	$0.763^{+0.016}_{-0.015}$
Eccentricity e	$0.30^{+0.03}_{-0.03}$
Inclination i (deg)	$116.1^{+0.5}_{-0.5}$
Arg. of periastron ω (deg)	$12.9^{+0.8}_{-0.8}$
Long. asc. node Ω (deg)	$169.3^{+0.5}_{-0.5}$
Periastron epoch $t_{\rm peri}$ (JD)	$2459523.6^{+7.0}_{-8.0}$
RV semi-amplitude K_1 (km s^{-1})	$16.9^{+0.9}_{-0.9}$

Notes. Uncertainties correspond to the posterior percentiles of the best-fit Keplerian model.

$\mu_{\rm Dec} = 2.762 \pm 0.038$ mas yr^{-1}, the lens proper motion is determined to be

$$\boldsymbol{\mu}_{\rm L,hel}({\rm N,E}) = (-3.3 \pm 0.5, 5.2 \pm 1.0)\,{\rm mas\,yr^{-1}}. \quad (12)$$

The heliocentric lens proper motion is related to the heliocentric lens velocity via

$$v_{\rm L,hel}\,[{\rm km\,s^{-1}}] = 4.74 \times D_{\rm L}\,\mu_{\rm L,hel}\,[{\rm mas\,yr^{-1}}], \quad (13)$$

where the 4.74 is a conversion factor from mas/yr to km/s. It is calculated to be

$$\boldsymbol{v}_{\rm L,hel}({\rm N,E}) = (-8.4 \pm 1.2, 13.2 \pm 2.9)\,{\rm km\,s^{-1}}, \quad (14)$$

which in Galactic coordinates equates to a lens velocity of

$$\boldsymbol{v}_{\rm L}({\rm l,b}) = (12.9 \pm 2.2, 8.9 \pm 3.0)\,{\rm km\,s^{-1}}. \quad (15)$$

5.5. Keplerian orbital motion

The Keplerian orbital motion parameters of the best-fit model (Table 3) are tightly constrained, as evidenced by the MCMC chains in Fig. B.1. We therefore investigate the physical parameters of the binary lens system as described by Skowron et al. (2011) and Bozza et al. (2021). Following their convention, the orbital parameters $(\gamma_1, \gamma_2, \gamma_3, r_s, a_s)$ are used to derive all elements of the bound elliptic orbital system and are listed in Table 5. The separation of the binary lens objects at periastron, $r_{t_{\rm peri}} = a(1-e) \simeq 0.5$ AU, and the kinematic vs potential check, $\beta_\perp = E_{\rm kin,\perp}/|E_{\rm pot}| \simeq 0.1 \leq 1.0$, imply a bound and physical orbit.

5.6. Follow-up observations

As the lens of the microlensing event is bright and the relative proper motion of the source and lens has been determined, we are able to determine when the source and lens will have an angular separation large enough to conduct follow-up observations of the binary lens. Radial-velocity follow-up has been used before to test microlensing models for binary lenses with orbital motion. The microlensing event OGLE-2009-BLG-020 (Skowron et al. 2011) estimated the full orbital parameters of a binary lens, which was followed up and confirmed by Yee et al. (2016). The microlensing event OGLE-2011-BLG-0417 (Shin et al. 2012) on the other hand was challenged by RV observations (Boisse et al. 2015) and high-resolution imaging (Santerne et al. 2016), which resulted in a refined model published in Bachelet et al. (2018).

Due to the large brightness contrast between the source and the lens in Gaia20fnr, follow-up observations aimed at isolating the lens light will require a substantial angular separation between the two objects. In seeing-limited observations, this would require a separation of approximately $\theta \gtrsim 1''$, whereas diffraction-limited high-angular-resolution imaging could become feasible at separations of $\theta \gtrsim 0.1''$. Using the estimated relative proper motion of the source and lens, these separations would be reached about 105 and 10.5 yr after t_0, respectively. Such high-angular-resolution imaging could help to resolve the source and lens, constrain the lens flux, and provide an independent check on the blend-light interpretation and relative proper motion.

The predicted radial-velocity semi-amplitude of the binary lens is large enough that RV observations could, in principle, provide an additional test of the microlensing model. However, such measurements will remain challenging because the lens is blended with a much brighter giant source. Radial-velocity follow-up may therefore become feasible only once the source and lens are sufficiently separated to reduce source contamination.

5.7. Gaia astrometry

Gaia DR4 will publish astrometric time series for all sources, which, for microlensing events brighter than about $G \lesssim 16$ mag will be of sufficient accuracy to detect the astrometric microlensing signal (Rybicki et al. 2018). The strength of using Gaia astrometry to test microlensing models has been demonstrated for the bright Gaia DR3 event GaiaDR3-ULENS-001, for which the anomalous Gaia DR3 astrometric solution can be explained by the astrometric microlensing signal implied by the photometric model (Jabłońska et al. 2022; Wyrzykowski et al. 2023). For the source of the microlensing event analysed in this study, which has an even brighter baseline magnitude of $m_{\rm G} = 13.11$ mag, the astrometric data will therefore allow a direct measurement of $\theta_{\rm E}$. Although the full astrometric signal that overlaps with the entire photometric event will not be published in Gaia DR4, the astrometric microlensing signal is observable well before and well after the photometric microlensing signal and could therefore be detectable with earlier data (Proft et al. 2011; Belokurov & Evans 2002). The astrometric time-series data released in DR4 will be from observations during the first 66 months of the mission, and could therefore already contain a detectable astrometric microlensing signal. We simulated the predicted astrometric signal based on the microlensing parameters from the photometric model. Together with the timestamps of predicted Gaia observations[7], it is shown in Fig. 10.

6. Conclusions

We analysed the triple-peaked, non-caustic-crossing binary microlensing event Gaia20fnr, whose complex morphology required a full Keplerian orbital motion model to reproduce the photometric data. The light curve contains data from four space telescopes (Gaia, NEOWISE, Swift, and TESS) as well as ground-based telescopes around the world coordinated through the BHTOM network. The photometric data were complemented by spectroscopic observations and by a set of parameters taken from Gaia DR3 to place constraints on the source.

[7] GOST: https://Gaia.esac.esa.int/gost/

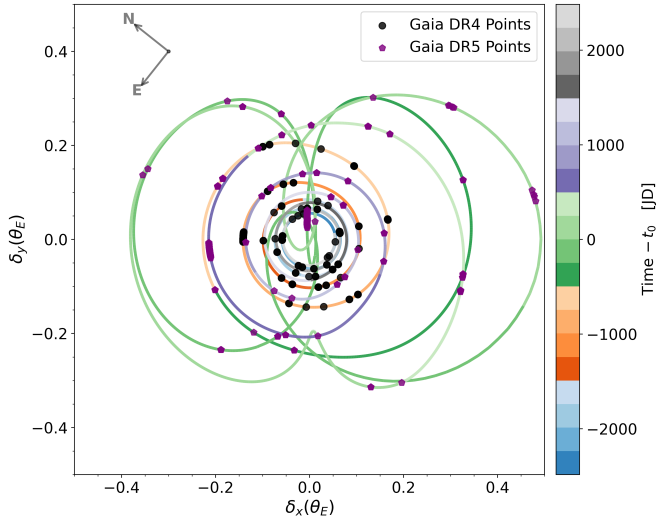


Fig. 10. Predicted centroid motion of the source of the Gaia20fnr microlensing event. The points marked as Gaia data were taken at timestamps determined with the Gaia Observation Forecast Tool (GOST).

Table 6. Key parameters of Gaia20fnr.

Event parameters	
D_S (pc)	3109 ± 105
D_L (pc)	536 ± 45
θ_E (mas)	3.50 ± 0.28
$\mu_{rel,geo}$(N, E) (mas yr^{-1})	$(-7.8 \pm 0.6, 16.6 \pm 1.3)$
$\mu_{S,hel}$(N, E) (mas yr^{-1})	$(2.72 \pm 0.01, -2.25 \pm 0.01)$
$\mu_{L,hel}$(N, E) (mas yr^{-1})	$(-3.3 \pm 0.5, 5.2 \pm 1.0)$
$M_{L,1}$ ($M_\odot$)	0.46 ± 0.06
$M_{L,2}$ ($M_\odot$)	0.52 ± 0.06
P (yr)	0.67 ± 0.04
K_1 (km s^{-1})	16.9 ± 0.9

Notes. Values summarise the source, lens, kinematic, and orbital parameters.

By incorporating information about the lens from the blend-flux in the best-fit microlensing model, we found that Gaia20fnr is best explained by a K2-type giant source at a distance of 3.1 kpc lensed by a binary system at 0.5 kpc. The lens consists of an early-M star ($M_{L,1} = 0.46 \pm 0.06\,M_\odot$) and a late-K star ($M_{L,2} = 0.52 \pm 0.06\,M_\odot$) orbiting each other with a period of 0.67 ± 0.04 years and a semi-major axis of 0.76 ± 0.02 AU. The Swift UV observations show a larger ratio of the measured flux coming from the source than for optical and IR observations. This is expected for the derived stellar parameters of the K2-type giant source star and the lens, as the UV emission is dominated by hotter stars. The kinematics of the microlensing event predict significant relative proper motion of the source and the lens and a measurable radial-velocity semi-amplitude. The main results are summarised in Table 6.

Gaia20fnr is one of only a handful of microlensing events for which a full Keplerian orbital solution has been derived and for which the results will be verifiable by follow-up observations. Upcoming Gaia DR4 and DR5 astrometric time-series data should provide a direct test of the lens-system architecture, while future radial-velocity monitoring and high-resolution imaging may offer complementary confirmation of the lens properties and source classification.

With the onset of deeper, high-cadence, and wide-area microlensing surveys such as the Vera C. Rubin Observatory's Legacy Survey of Space and Time (LSST) (Sajadian & Poleski 2019) and the Nancy Grace Roman Space Telescope (Penny et al. 2019), the discovery rate of long, complex, and parallax- or orbital-motion-dominated microlensing events will increase dramatically. Events such as Gaia20fnr demonstrate that densely sampled, multi-mission photometry combined with source constraints from spectroscopy and the Gaia DR3 catalogue enable precise characterisations of nearby binary lenses, including complete orbital solutions. Additionally, future space-based missions, such as the proposed GaiaNIR mission (Hobbs & Høg 2018) that will be the next generation astrometric survey providing unique and ultra-precise astrometric time-series, could offer the precision necessary to break common microlensing degeneracies. Thus, such future missions will enable secure physical characterisations of complex microlensing events such as the one presented in this study.

Data availability

The reduced SPRAT, GMOS-N, and FLOYDS spectra of Gaia20fnr are available at the CDS via https://cdsarc.cds.unistra.fr/viz-bin/cat/J/A+A/710/A294

Acknowledgements. BHTOM.space is based on the open-source TOM Toolkit by LCO and has been developed with funding from the OPTICON-RadioNet Pilot (ORP) of the European Union's Horizon 2020 research and innovation programme under grant agreement No 101004719 (2021–2025). This project has received funding from the European Union's Horizon Europe Research and Innovation programme ACME under grant agreement No 101131928 (2024–2028). Ł.W. acknowledges support from the Polish National Science Centre DAINA grant No 2024/52/L/ST9/00210. E.S., M.M., J.Z., E.P., V.C., and U.J. acknowledge funding from the Research Council of Lithuania (LMTLT, grant No. S-LL-24-1). This work makes use of observations from the Las Cumbres Observatory global telescope network. Support for this project is provided by ANID's Millennium Science Initiative through grant ICN12_009, awarded to the Millennium Institute of Astrophysics (MAS), and by ANID's Basal project FB210003. YT acknowledges the support of DFG priority program SPP 1992 "Exploring the Diversity of Extrasolar Planets" (TS 356/3-1). RAS and EB gratefully acknowledge support from the NASA XRP Program, through grant number 80NSSC19K0291. This work was authored by employees of Caltech/IPAC under Contract No. 80GSFC21R0032 with the National Aeronautics and Space Administration. This project has received funding from the European Union's Horizon 2020 research and innovation program under grant agreement No. 101004719 (OPTICON – RadioNet Pilot). This work is supported by the Polish MNiSW grant DIR/WK/2018/12. Partial support for MR is provided by the Dirección de Investigación of the Universidad Católica de la Santísima Concepción with the project DIREG 10/2023 and by ANID with the project QUIMAL230011. KK greatly acknowledges the support from the NSF AAG program, through grant number 2206828. The research of JMe was supported by the Czech Science Foundation (GACR) project no. 24-10608O. This work is partially supported by the Fundamental Fund of Thailand Science Research and Innovation (TSRI) through the National Astronomical Research Institute of Thailand (Public Organization) (FFB690078/0269). The Liverpool Telescope is operated on the island of La Palma by Liverpool John Moores University in the Spanish Observatorio del Roque de los Muchachos of the Instituto de Astrofisica de Canarias with financial support from the UK Science and Technology Facilities Council. Based on observations obtained at the international Gemini Observatory, a program of NSF NOIRLab, which is managed by the Association of Universities for Research in Astronomy (AURA) under a cooperative agreement with the U.S. National Science Foundation on behalf of the Gemini Observatory partnership: the U.S. National Science Foundation (United States), National Research Council (Canada), Agencia Nacional de Investigación y Desarrollo (Chile), Ministerio de Ciencia, Tecnología e Innovación (Argentina), Ministério da Ciência, Tecnologia, Inovações e Comunicações (Brazil), and Korea Astronomy and Space Science Institute (Republic of Korea). This work was enabled by observations made from the Gemini North telescope, located within the Maunakea Science Reserve and adjacent to the summit of Maunakea. We are grateful for the privilege of observing the Universe from a place that is unique in both its astronomical quality and its cultural significance. D.A.H.B. acknowledges support from the

South African National Research Foundation. Some of the observations reported in this paper were obtained with the Southern African Large Telescope (SALT). Polish participation in SALT is funded by grants No. MEiN 2021/WK/01 and MNiSW DIR/WK/2016/07. Based on observations collected at the European Southern Observatory under ESO programme 108.22JZ.001. We thank the Neil Gehrels Swift Observatory team for promptly approving and executing our Target of Opportunity observations. M.W. thanks Mateusz Jan Mróz and the Microlensing Journal Club at OAUW for helpful discussions regarding the modelling of the light curve.

References

Abrams, N. S., Lu, J. R., Lam, C. Y., et al. 2025, ApJ, 980, 103
Albrow, M. D., Beaulieu, J., Caldwell, J. A. R., et al. 1999, ApJ, 522, 1022
Albrow, M. D., Beaulieu, J., Caldwell, J. A. R., et al. 2000, ApJ, 534, 894
Alcock, C., Allsman, R. A., Axelrod, T. S., et al. 1996, ApJ, 461, 84
Andersen, J., Andersen, M. I., Klougart, J., et al. 1995, The Messenger, 79, 12
Astropy Collaboration (Robitaille, T. P., et al.) 2013, A&A, 558, A33
Bachelet, E., Shin, I.-G., Han, C., et al. 2012, ApJ, 754, 73
Bachelet, E., Norbury, M., Bozza, V., & Street, R. 2017, arXiv e-prints [arXiv:1709.08704]
Bachelet, E., Beaulieu, J.-P., Boisse, I., Santerne, A., & Street, R. A. 2018, ApJ, 865, 162
Bachelet, E., Tsapras, Y., Gould, A., et al. 2022, AJ, 164, 75
Bachelet, E., Hundertmark, M., & Calchi Novati, S. 2024a, AJ, 168, 24
Bachelet, E., Rota, P., Bozza, V., et al. 2024b, AJ, 168, 9
Bailer-Jones, C. A. L., Rybizki, J., Fouesneau, M., Demleitner, M., & Andrae, R. 2021, AJ, 161, 147
Beaulieu, J.-P., Bennett, D. P., Fouqué, P., et al. 2006, Nature, 439, 437
Bellm, E. C., Kulkarni, S. R., Graham, M. J., et al. 2019, PASP, 131, 018002
Belokurov, V. A., & Evans, N. W. 2002, MNRAS, 331, 649
Bennett, D. P., Anderson, J., & Gaudi, B. S. 2007, ApJ, 660, 781
Bennett, D. P., Rhie, S. H., Udalski, A., et al. 2016, AJ, 152, 125
Bensby, T., Yee, J. C., Feltzing, S., et al. 2013, A&A, 549, A147
Bessell, M. S. 1990, PASP, 102, 1181
Blanco-Cuaresma, S. 2019, MNRAS, 486, 2075
Blanco-Cuaresma, S., Soubiran, C., Heiter, U., & Jofré, P. 2014, A&A, 569, A111
Boffin, H. M. J., & Jones, D. 2024, arXiv e-prints [arXiv:2411.18470]
Boisse, I., Santerne, A., Beaulieu, J.-P., et al. 2015, A&A, 582, L11
Bond, I. A., Abe, F., Dodd, R. J., et al. 2001, MNRAS, 327, 868
Bond, I. A., Udalski, A., Jaroszyński, M., et al. 2004, ApJ, 606, L155
Bonnarel, F., Fernique, P., Bienaymé, O., et al. 2000, A&AS, 143, 33
Bovy, J. 2015, ApJS, 216, 29
Bozza, V. 2001, A&A, 374, 13
Bozza, V., Khalouei, E., & Bachelet, E. 2021, MNRAS, 505, 126
Bozza, V., Saggese, V., Covone, G., Rota, P., & Zhang, J. 2025, A&A, 694, A219
Bramich, D. M. 2008, MNRAS, 386, L77
Bramich, D. M., Horne, K., Albrow, M. D., et al. 2013, MNRAS, 428, 2275
Bressan, A., Marigo, P., Girardi, L., et al. 2012, MNRAS, 427, 127
Brown, T. M., Baliber, N., Bianco, F. B., et al. 2013, PASP, 125, 1031
Buckley, D. A. H., Swart, G. P., & Meiring, J. G. 2006, SPIE Conf. Ser., 6267, 62670Z
Campbell, H. C., Marsh, T. R., Fraser, M., et al. 2015, MNRAS, 452, 1060–1067
Cardelli, J. A., Clayton, G. C., & Mathis, J. S. 1989, ApJ, 345, 245
Casares, J., & Jonker, P. G. 2014, Space Sci. Rev., 183, 223
Cassan, A. 2008, A&A, 491, 587
Chambers, K. C., Magnier, E. A., Metcalfe, N., et al. 2019, arXiv e-prints [arXiv:1612.05560]
Crause, L. A., Sharples, R. M., Bramall, D. G., et al. 2014, SPIE Conf. Ser., 9147, 91476T
Czekaj, M. A., Robin, A. C., Figueras, F., Luri, X., & Haywood, M. 2014, A&A, 564, A102
Di Stefano, R., & Esin, A. 2014, arXiv e-prints [arXiv:1412.7675]
Dominik, M. 1999, arXiv e-prints [arXiv:astro-ph/9903014]
Dominik, M. 2006, MNRAS, 367, 669
Dong, S., Udalski, A., Gould, A., et al. 2007, ApJ, 664, 862
Dong, S., Gould, A., Udalski, A., et al. 2009, ApJ, 695, 970
Dong, S., Wu, Z., Ryu, Y.-H., et al. 2026, Science, 391, 96
Drake, A. J., Djorgovski, S. G., Mahabal, A., et al. 2009, ApJ, 696, 870
Drake, A. J., Djorgovski, S. G., Mahabal, A., et al. 2012, in IAU Symposium, 285, New Horizons in Time Domain Astronomy, eds. E. Griffin, R. Hanisch, & R. Seaman, 306
Erdl, H., & Schneider, P. 1993, A&A, 268, 453
Foreman-Mackey, D. 2016, J. Open Source Softw., 1, 24
Foreman-Mackey, D., Hogg, D. W., Lang, D., & Goodman, J. 2013, PASP, 125, 306
Fukugita, M., Ichikawa, T., Gunn, J. E., et al. 1996, AJ, 111, 1748
Gaia Collaboration (Brown, A. G. A., et al.) 2021, A&A, 649, A1
Gaia Collaboration (Montegriffo, P., et al.) 2023a, A&A, 674, A33
Gaia Collaboration (Vallenari, A., et al.) 2023b, A&A, 674, A1
Gaudi, B. S. 2012, ARA&A, 50, 411
Gaudi, B. S., & Gould, A. 1999, ApJ, 513, 619
Gould, A. 1994, ApJ, 421, L75
Gould, A. 2004, ApJ, 606, 319
Grevesse, N., Asplund, M., & Sauval, A. J. 2007, Space Sci. Rev., 130, 105
Guo, X., Esin, A., Stefano, R. D., & Taylor, J. 2015, ApJ, 809, 182
Gustafsson, B., Edvardsson, B., Eriksson, K., et al. 2008, A&A, 486, 951
Hambsch, F.-J. 2012, J. Am. Assoc. Variable Star Observers, 40, 1003
Hobbs, D., & Høg, E. 2018, in IAU Symposium, 330, Astrometry and Astrophysics in the Gaia Sky, eds. A. Recio-Blanco, P. de Laverny, A. G. A. Brown, & T. Prusti, 67
Hodgkin, S. T., Breedt, E., Delgado, A., et al. 2020, Transient Name Server Discovery Report, 2020-3645, 1
Hodgkin, S. T., Harrison, D. L., Breedt, E., et al. 2021, A&A, 652, A76
Hook, I. M., Jørgensen, I., Allington-Smith, J. R., et al. 2004, PASP, 116, 425
Houdashelt, M. L., Bell, R. A., Sweigart, A. V., & Wing, R. F. 2000, AJ, 119, 1424
Howil, K., Wyrzykowski, Ł., Kruszyńska, K., et al. 2025, A&A, 694, A94
Jabłońska, M., Wyrzykowski, Ł., Rybicki, K. A., et al. 2022, A&A, 666, L16
Jankovič, T., Gomboc, A., Wyrzykowski, Ł., et al. 2025, A&A, 699, A156
Jaroszyński, M., & Mao, S. 2001, MNRAS, 325, 1546
Jordi, K., Grebel, E. K., & Ammon, K. 2006, A&A, 460, 339
Kaczmarek, Z., McGill, P., Perkins, S. E., et al. 2025, ApJ, 981, 183
Kangas, T., Blagorodnova, N., Mattila, S., et al. 2017, MNRAS, 469, 1246
Kim, S.-L., Lee, C.-U., Park, B.-G., et al. 2016, J. Korean Astron. Soc., 49, 37
Kniazev, A. Y., Gvaramadze, V. V., & Berdnikov, L. N. 2016, MNRAS, 459, 3068
Kniazev, A. Y., Gvaramadze, V. V., & Berdnikov, L. N. 2017, in Astronomical Society of the Pacific Conference Series, 510, Stars: From Collapse to Collapse, eds. Y. Y. Balega, D. O. Kudryavtsev, I. I. Romanyuk, & I. A. Yakunin, 480
Kochanek, C. S., Shappee, B. J., Stanek, K. Z., et al. 2017, PASP, 129, 104502
Kostrzewa-Rutkowska, Z., Jonker, P. G., Hodgkin, S. T., et al. 2018, MNRAS, 481, 307
Kostrzewa-Rutkowska, Z., Jonker, P. G., Hodgkin, S. T., et al. 2020, MNRAS, 493, 3264
Kruszyńska, K., Wyrzykowski, Ł., Rybicki, K. A., et al. 2022, A&A, 662, A59
Kruszyńska, K., Wyrzykowski, Ł., Rybicki, K. A., et al. 2024, A&A, 692, A28
Kunimoto, M., DeRocco, W., Smyth, N., Bryson, S., & Gaudi, B. S. 2025, Searching for Free-Floating Planets with TESS: Results from Sectors 61–65
Lam, C. Y., Lu, J. R., Udalski, A., et al. 2022, ApJ, 933, L23
Law, N. M., Kulkarni, S. R., Dekany, R. G., et al. 2009, PASP, 121, 1395
Mainzer, A., Grav, T., Bauer, J., et al. 2011, ApJ, 743, 156
Mao, S., & Paczynski, B. 1991, ApJ, 374, L37
Marshall, D. J., Robin, A. C., Reylé, C., Schultheis, M., & Picaud, S. 2006, A&A, 453, 635
Martin, D. C., Fanson, J., Schiminovich, D., et al. 2005, ApJ, 619, L1
Maskoliūnas, M., Wyrzykowski, Ł., Howil, K., et al. 2024, Acta Astron., 74, 77
McCully, C., Volgenau, N. H., Harbeck, D.-R., et al. 2018, SPIE Conf. Ser., 10707, 107070K
Merc, J., Mikołajewska, J., Gromadzki, M., et al. 2020, A&A, 644, A49
Merc, J., Velez, P., Charbonnel, S., et al. 2024, Astron. Nachr., 345, e20240017
Mikolajczyk, P. J., Zieliński, P., Wyrzykowski, L., Krawczyk, A., & Kotysz, K. 2025, in Revista Mexicana de Astronomia y Astrofisica Conference Series, 59, 167
Mints, A., & Hekker, S. 2017, A&A, 604, A108
Mints, A., & Hekker, S. 2018, A&A, 618, A54
Mistry, D., Copperwheat, C. M., Darnley, M. J., & Olier, I. 2022, MNRAS, 517, 3362
Miyake, N., Udalski, A., Sumi, T., et al. 2012, ApJ, 752, 82
Moe, M., & Di Stefano, R. 2017, ApJS, 230, 15
Morales, J. C., Ribas, I., Giménez, Á., & Baroch, D. 2022, Galaxies, 10, 98
Mróz, P. 2024, Acta Astron., 73, 259
Mróz, P., Ryu, Y.-H., Skowron, J., et al. 2018, AJ, 155, 121
Mróz, P., Udalski, A., Bennett, D. P., et al. 2019, A&A, 622, A201
Mróz, P., Udalski, A., Szymański, M. K., et al. 2025, ApJS, 280, 49
Nasa High Energy Astrophysics Science Archive Research Center (HEASARC). 2014, HEAsoft: Unified Release of FTOOLS and XANADU, Astrophysics Source Code Library [record ascl:1408.004]
Nataf, D. M., Gould, A., Fouqué, P., et al. 2013, ApJ, 769, 88
Nguyen, C. T., Costa, G., Girardi, L., et al. 2022, A&A, 665, A126
Nicholl, M., Berger, E., Margutti, R., et al. 2017, ApJ, 835, L8

Nucita, A. A., Giordano, M., De Paolis, F., & Ingrosso, G. 2014, MNRAS, 438, 2466
Oliveira, R. A. P., Poleski, R., Mróz, P., et al. 2025, arXiv e-prints [arXiv:2504.21085]
Paczynski, B. 1986, ApJ, 304, 1
Paczyński, B. 1971, ARA&A, 9, 183
Penny, M. T., Kerins, E., & Mao, S. 2011a, MNRAS, 417, 2216
Penny, M. T., Mao, S., & Kerins, E. 2011b, MNRAS, 412, 607
Penny, M. T., Kerins, E., Rattenbury, N., et al. 2013, MNRAS, 434, 2
Penny, M. T., Gaudi, B. S., Kerins, E., et al. 2019, ApJS, 241, 3
Pessi, P. J., Lunnan, R., Sollerman, J., et al. 2025, MNRAS, 542, 3354
Piascik, A. S., Steele, I. A., Bates, S. D., et al. 2014, SPIE Conf. Ser., 9147, 91478H
Poleski, R., Skowron, J., Mróz, P., et al. 2021, Acta Astron., 71, 1
Popper, D. M. 1967, ARA&A, 5, 85
Proft, S., Demleitner, M., & Wambsganss, J. 2011, A&A, 536, A50
Pylypenko, U., Wyrzykowski, Ł., Mikołajczyk, P. J., et al. 2026, A&A, 705, A24
Raghavan, D., McAlister, H. A., Henry, T. J., et al. 2010, ApJS, 190, 1
Rattenbury, N. J., Bond, I. A., Skuljan, J., & Yock, P. C. M. 2002, MNRAS, 335, 159
Refsdal, S. 1966, MNRAS, 134, 315
Reichart, D., Nysewander, M., Moran, J., et al. 2005, Nuovo Cimento C Geophys. Space Phys. C, 28, 767
Ricker, G. R., Winn, J. N., Vanderspek, R., et al. 2015, J. Astron. Telesc. Instrum. Syst., 1, 014003
Robin, A. C., Reylé, C., Derrière, S., & Picaud, S. 2003, A&A, 409, 523
Roming, P. W. A., Kennedy, T. E., Mason, K. O., et al. 2005, Space Sci. Rev., 120, 95
Ropert, S., Rojas, R., Suc, V., et al. 2021, in Revista Mexicana de Astronomia y Astrofisica Conference Series, 53, 47
Rota, P., Bozza, V., Hundertmark, M., et al. 2024, A&A, 686, A173
Rybicki, K. A., Wyrzykowski, Ł., Klencki, J., et al. 2018, MNRAS, 476, 2013
Rybicki, K. A., Wyrzykowski, Ł., Bachelet, E., et al. 2022, A&A, 657, A18
Sahu, K. C., Anderson, J., Casertano, S., et al. 2022, ApJ, 933, 83
Sajadian, S., & Poleski, R. 2019, ApJ, 871, 205
Salgado, C., & McDavid, D. 2008, in American Astronomical Society Meeting Abstracts, 212, 24.02
Sajadian, S., Kalantari, A., Fatheddin, H., & Khakpash, S. 2025, AJ, 169, 34
Santerne, A., Beaulieu, J.-P., Rojas Ayala, B., et al. 2016, A&A, 595, L11
Schlafly, E. F., & Finkbeiner, D. P. 2011, ApJ, 737, 103
Schlegel, D. J., Finkbeiner, D. P., & Davis, M. 1998, ApJ, 500, 525
Sergeev, A., & Tarady, V. 2007, Bulg. Astron. J., 9, 121
Shin, I.-G., Han, C., Choi, J.-Y., et al. 2012, ApJ, 755, 91
Skowron, J., Jaroszynski, M., Udalski, A., et al. 2007, Acta Astron., 57, 281
Skowron, J., Udalski, A., Gould, A., et al. 2011, ApJ, 738, 87
Skrutskie, M. F., Cutri, R. M., Stiening, R., et al. 2006, AJ, 131, 1163
Stassun, K. G., Oelkers, R. J., Paegert, M., et al. 2019, AJ, 158, 138
Steele, I. A., Smith, R. J., Rees, P. C., et al. 2004, SPIE Conf. Ser., 5489, 679
Storn, R., & Price, K. 1997, J. Global Optim., 11, 341
Straižys, V. 1992, Multicolor Stellar Photometry (Tucson: Pachart Pub. House)
Street, R. A., Bowman, M., Saunders, E. S., & Boroson, T. 2018, SPIE Conf. Ser., 10707, 1070711
Street, R. A., Bachelet, E., Tsapras, Y., et al. 2024a, PASP, 136, 064501
Street, R. A., Lindstrom, W., Heinrich-Josties, E., et al. 2024b, in Astronomical Society of the Pacific Conference Series, 535, Astronomical Data Analysis Software and Systems XXXI, eds. B. V. Hugo, R. Van Rooyen, & O. M. Smirnov, 3
Sumi, T., Buckley, D. A. H., Kutyrev, A. S., et al. 2025, AJ, 170, 338
Sweeney, D., Tuthill, P., Krone-Martins, A., et al. 2024, MNRAS, 531, 2433
Szkudlarek, M., & żejmo, M. 2024, in Proceedings of the XLI Polish Astronomical Society Meeting, 13, 273
Tonry, J. L., Denneau, L., Heinze, A. N., et al. 2018, PASP, 130, 064505
Torres, G., Andersen, J., & Giménez, A. 2010, A&A Rev., 18, 67
Udalski, A., Kubiak, M., & Szymanski, M. 1997, Acta Astron., 47, 319
Udalski, A., Zebrun, K., Szymanski, M., et al. 2000, Acta Astron., 50, 1
Udalski, A., Han, C., Bozza, V., et al. 2018, ApJ, 853, 70
Udalski, A., Yee, J. C., Gould, A., et al. 2015, ApJ, 799, 237
Vernet, J., Dekker, H., D'Odorico, S., et al. 2011, A&A, 536, A105
Werner, M. W., Roellig, T. L., Low, F. J., et al. 2004, ApJS, 154, 1
Witt, H. J., & Mao, S. 1994, ApJ, 430, 505
Wright, E. L., Eisenhardt, P. R. M., Mainzer, A. K., et al. 2010, AJ, 140, 1868
Wyrzykowski, L. 2024, in What Was That? – Planning ESO Follow up for Transients, Variables, and Solar System Objects in the Era of LSST, 4
Wyrzykowski, Ł., Kostrzewa-Rutkowska, Z., Skowron, J., et al. 2016, MNRAS, 458, 3012
Wyrzykowski, Ł., Mróz, P., Rybicki, K. A., et al. 2020, A&A, 633, A98
Wyrzykowski, Ł., Kruszyńska, K., Rybicki, K. A., et al. 2023, A&A, 674, A23
Yang, H., Zang, W., Gan, T., et al. 2024, ApJ, 972, L12
Yee, J. C., Shvartzvald, Y., Gal-Yam, A., et al. 2012, ApJ, 755, 102
Yee, J. C., Udalski, A., Novati, S. C., et al. 2015, ApJ, 802, 76
Yee, J. C., Johnson, J. A., Skowron, J., et al. 2016, ApJ, 821, 121
Yoo, J., DePoy, D. L., Gal-Yam, A., et al. 2004, ApJ, 603, 139
Zerbi, F. M., Chincarini, G., Ghisellini, G., et al. 2004, SPIE Conf. Ser., 5492, 1590
Zieliński, P., Wyrzykowski, Ł., Rybicki, K., et al. 2019, Contrib. Astron. Observ. Skal. Pleso, 49, 125
Zielinski, P., Wyrzykowski, L., Mikolajczyk, P., Rybicki, K., & Kolaczkowski, Z. 2020, Towards an automatic processing of CCD images with CPCS 2.0
Zielinski, P., Gezer, I., Gromadzki, M., et al. 2021, Astronomer's Telegram, 14316, 1
Zub, M., Cassan, A., Heyrovský, D., et al. 2011, A&A, 525, A15

[1] Astronomical Observatory, University of Warsaw, Al. Ujazdowskie 4, 00-478 Warsaw, Poland
[2] Isaac Newton Group of Telescopes, Apartado 321, 38700 Santa Cruz de La Palma, Spain
[3] Astrophysics Division, National Centre for Nuclear Research, Pasteura 7, 02-093, Warsaw, Poland
[4] Astronomisches Rechen-Institut, Zentrum für Astronomie der Universität Heidelberg (ZAH), 69120 Heidelberg, Germany
[5] Institute of Astronomy, Faculty of Physics, Astronomy and Informatics, Nicolaus Copernicus University, Grudziądzka 5, 87-100 Toruń, Poland
[6] Vilnius University, Faculty of Physics, Institute of Theoretical Physics and Astronomy, Sauletekio av. 3, 10257 Vilnius, Lithuania
[7] Université Marie et Louis Pasteur, CNRS, Institut UTINAM UMR 6213, Besançon, France
[8] Las Cumbres Observatory, 6740 Cortona Drive, Suite 102, 93117 Goleta, CA, USA
[9] SUPA, School of Physics & Astronomy, University of St Andrews, North Haugh, St Andrews KY16 9SS, UK
[10] South African Astronomical Observatory, PO Box 9, Observatory 7935, Cape Town, South Africa
[11] Department of Astronomy, University of Cape Town, Private Bag X3, Rondebosch 7701, South Africa
[12] Institute for Machine Learning, Johannes Kepler University Linz, Altenberger Straße 69, 694040 Linz, Austria
[13] NSF NOIRLab, 670 N. A'ohoku Place, Hilo, HI 96720, USA
[14] Astronomical Institute, University of Wrocław, ul. Mikołaja Kopernika 11, 51-622 Wrocław, Poland
[15] Dipartimento di Fisica "E.R. Caianiello", Università di Salerno, Via Giovanni Paolo II 132, 84084 Fisciano, Italy
[16] Istituto Nazionale di Fisica Nucleare, Sezione di Napoli, Via Cintia, 80126 Napoli, Italy
[17] Institut d'Astrophysique de Paris, Sorbonne Université, CNRS, UMR 7095, 98 bis bd Arago, 75014 Paris, France
[18] Millennium Institute of Astrophysics MAS, Nuncio Monsenor Sotero Sanz 100, Of. 104, Providencia, Santiago, Chile
[19] Instituto de Astrofísica, Facultad de Física, Pontificia Universidad Católica de Chile, Av. Vicuña Mackenna 4860, 7820436 Macul, Santiago, Chile
[20] Departamento de Matemática y Física Aplicadas, Facultad de Ingeniería, Universidad Católica de la Santísima Concepción, Alonso de Rivera 2850, Concepción, Chile
[21] National Astronomical Research Institute of Thailand (Public Organization), 260 Moo 4, Donkaew, Mae Rim, Chiang Mai 50180, Thailand
[22] Flarestar Observatory, FL5 Ent.B, Silver Jubilee Apt, George Tayar Street, San Gwann, SGN 3160, Malta
[23] Department of Astronomy, University of Virginia, 530 McCormick Road, Charlottesville, VA 22904, USA
[24] British Astronomical Association, PO Box 702, Tonbridge, TN9 9TX England

[25] Institute of Earth Systems, University of Malta, Msida MSD 2080, Malta
[26] Znith Astronomy Observatory, 31, Armonie, E. Bradford Street, Naxxar 2217, Malta
[27] International Center for Astronomical and Medico-Ecological Research (ICAMER), National Academy of Sciences of Ukraine, 27 Acad. Zabolotnoho Str., Kyiv 03143, Ukraine
[28] Vereniging Voor Sterrenkunde (VVS), Zeeweg 96, B-8200 Brugge, Belgium
[29] Bundesdeutsche Arbeitsgemeinschaft für Veränderliche Sterne, Munsterdamm 90, 12169 Berlin, Germany
[30] Research School of Astronomy and Astrophysics, Australian National University, Mount Stromlo Observatory, Cotter Road Weston Creek, ACT 2611, Australia
[31] Faculty of Automatic Control, Electronics and Computer Science, Silesian University of Technology, Akademicka 16, 44-100 Gliwice, Poland
[32] E. Kharadze Georgian National Astrophysical Observatory, 0301 Abastumani, Georgia
[33] Center for Astrophysics and Cosmology, University of Nova Gorica, Vipavska 11c, 5270 Ajdovščina, Slovenia
[34] Argelander-Institut für Astronomie, Universität Bonn, Auf dem Hügel 71, 53121 Bonn, Germany
[35] Instytut Fizyki im. Mariana Smoluchowskiego, Uniwersytet Jagielloński, ul. prof. St. Łojasiewicza 11, 30-348 Kraków, Poland
[36] Institute of Physics, Faculty of Science, Pavol Jozef Šafárik University in Košice, Park Angelinum 9, 040 01 Košice, Slovakia
[37] Astronomical Institute of Charles University, V Holešovičkách 2, Prague 18000, Czech Republic
[38] Instituto de Astrofísica de Canarias, Calle Vía Láctea, s/n 38205 La Laguna, Tenerife, Spain
[39] Janusz Gil Institute of Astronomy, University of Zielona Góra, Szafrana 2, 65-516 Zielona Góra, Poland
[40] Department of Physics and Astronomy, University of North Carolina at Chapel Hill, Chapel Hill, NC 27599, USA
[41] American Association of Variable Star Observers (AAVSO), 185 Alewife Brook Parkway, Suite 410, Cambridge, MA 02138, USA
[42] Astronomy and Space Physics Department, Taras Shevchenko National University of Kyiv, 4 Glushkova ave., Kyiv, 03022, Ukraine
[43] National Center "Junior Academy of Sciences of Ukraine", 38-44 Dehtiarivska St., Kyiv, 04119, Ukraine
[44] Astronomical Observatory, Jagiellonian University, ul. Orla 171, 30-244 Kraków, Poland

Appendix A: Photometric data and follow-up

Table A.1 contains all the information about the telescopes and instruments involved in the ground-based follow-up observations of the Gaia20fnr microlensing event. The data for the follow-up observations were processed by the BHTOM tool (Wyrzykowski 2024). Table A.2 contains information on the observations made with all telescopes, including the ground-based follow-up observations, surveys, and space telescopes, in connection with the Gaia20fnr event.

Table A.1. Ground-based follow-up instruments.

Telescope code	Telescope/observatory name	Location	Long. [deg]	Lat. [deg]	Alt. [m]	Reference
Abastumani-150	Georgian National Astrophysical Observatory	Abastumani, Georgia	42.8	41.8	1650	-
Adiyaman-60	Adiyaman Observatory	Adiyaman, Turkey	38.2	37.8	600	-
BGO-60	Burke-Gaffney Observatory	Halifax, Canada	-63.6	44.6	93	-
Danish-154	La Silla Observatory	La Silla, Chile	-70.7	-29.3	2375	Andersen et al. (1995)
Flarestar-25	Flarestar Observatory	San Gwann, Malta	14.5	35.9	126	-
GoChile-40	El Sauce Observatory	Río Hurtado Valley, Chile	-70.8	-30.5	1560	Ropert et al. (2021)
LCO-cpt-100	LCO - South African Astronomical Observatory	Sutherland, South Africa	20.8	-32.4	1760	Brown et al. (2013)
LCO-lsc-100	LCO - Cerro Tololo Inter-American Observatory	Cerro Tololo, Chile	-70.8	-30.2	2201	Brown et al. (2013)
LCO-coj-100	LCO - Siding Spring Observatory	Siding Spring, Australia	149.1	-31.3	1165	Brown et al. (2013)
LCO-elp-100	LCO - McDonald Observatory	Jeff Davis County, Texas	-104.0	30.7	2077	Brown et al. (2013)
LCO-tfn-100	LCO - Teide Observatory	Tenerife	-16.5	28.3	2390	Brown et al. (2013)
PROMPT-MO-1-40	Meckering Observatory	Meckering, Australia	117.0	-31.6	650	Reichart et al. (2005)
PROMPT5-41	Cerro Tololo Inter-American Observatory	Cerro Tololo, Chile	-70.8	-30.2	2286	Reichart et al. (2005)
PROMPT6-40	Cerro Tololo Inter-American Observatory	Cerro Tololo, Chile	-70.8	-30.2	2286	Reichart et al. (2005)
REM-60	La Silla Observatory	La Silla, Chile	-70.7	-29.3	2400	Zerbi et al. (2004)
ROAD-40	Remote Observatory Atacama Desert	San Pedro de Atacama, Chile	-68.2	-23.0	2500	Hambsch (2012)
RRRT-60	Fan Mountains Observatory	Virginia, USA	-78.7	37.9	1683	Salgado & McDavid (2008)
SUTO-Otivar-30	Silesian University of Technology Observatories	Granada, Spain	-3.7	36.8	200	-
TRT-SBO-70	Thai Robotic Telescopes, Spring Brook Observatory	Springbrook, Queensland, Australia	149.1	-31.3	1020	-
Terskol-60	Terskol Observatory	Terskol, North Caucasus	42.5	43.3	3143	Sergeev & Tarady (2007)
Terskol-200	Terskol Observatory	Terskol, North Caucasus	42.5	43.3	3143	Sergeev & Tarady (2007)
UZPW-50	University of Zielona Góra PlaneWave L500	Badajoz, Spain	-6.6	38.2	560	Szkudlarek & żejmo (2024)
Warrumbungle-51	Warrumbungle Observatory	Siding Spring, Australia	149.2	-31.3	552	-
ZAO-20	Znith Astronomy Observatory	Malta	14.4	35.9	113	-

Notes. The table lists telescope codes, observatories, locations, coordinates, altitudes, and references.

Table A.2. Observation time ranges and filter counts.

Telescope code	First epoch [MJD]	Last epoch [MJD]	Number of points (filter)
Abastumani-150	59510.54	59527.48	13(V),12(r),6(I),2(i)
Adiyaman-60	59256.32	59319.20	4(g),2(I),2(R),2(r),1(z)
BGO-60	59478.35	59640.00	27(V),26(B),26(I),26(R)
Danish-154	59533.65	59867.73	8(R),8(V),7(I),6(B)
Flarestar-25	59542.45	59636.27	11(V),8(I)
GoChile-40	60025.56	60029.55	9(g),6(V),6(r)
LCO-cpt-100	59206.83	60029.73	415(i),306(g),3(B),1(I),1(R)
LCO-lsc-100	59209.21	60034.98	442(i),324(g),6(B),1(I),1(U),1(u)
LCO-coj-100	59205.56	60027.40	252(i),167(g)
LCO-elp-100	59215.24	59849.49	19(i),13(g)
LCO-tfn-100	59472.24	59576.00	27(i),16(g)
PROMPT-MO-1-40	59288.97	59770.41	3(V),2(I),2(r),1(i)
PROMPT5-41	59680.49	59905.85	16(g),15(i),15(r),4(V),2(I),1(R)
PROMPT6-40	59277.62	59296.61	33(V),29(I),21(R),12(r),3(i)
REM-60	59243.57	60035.57	1014(i),932(r),762(z),616(g),536(V),398(R),245(I),4(B),1(u)
ROAD-40	59233.55	59646.53	2346(V),2188(B),2121(I),81(R),3(U)
RRRT-60	59843.92	59861.92	2(g),2(i),2(r)
SUTO-Otivar-30	59828.68	60037.34	66(B),57(V),57(r),45(I),14(R),10(i),2(g)
TRT-SBO-70	59221.95	59471.18	64(V),41(I),15(R),3(r),1(i)
Terskol-60	59621.33	59635.29	8(g),7(R),7(V),6(I),1(z)
Terskol-200	59465.55	59629.31	24(V),18(R),17(g),15(I),13(r),8(i),7(B),7(z),1(u)
UZPW-50	59908.71	60043.48	147(g),145(r),133(i),14(V),11(B),9(R)
Warrumbungle-51	59249.03	59260.06	1(B),1(R),1(V),1(r)
ZAO-20	59579.48	59649.37	58(I),44(V)
ASAS-SN	56593.58	60713.11	3022(g),852(V)
ATLAS	57297.56	60347.92	2563(o),670(c),4(g),3(r),1(H)
ZTF	58439.27	60286.35	90(zr),80(zg)
Gaia	57069.56	60325.48	255(G)
NEOWISE	56734.61	60369.00	354(W2),353(W1)
Swift	59327.64	59657.45	17(B),17(U),17(UVW1),16(UVW2),16(V)
TESS	58467.79	60689.44	15633(TESS)

Notes. First and last epochs are in MJD. Counts are given as the number of data points per filter.

Appendix B: Fit convergence

Fig. B.1 contains the confidence contours of MCMC-derived binary-lens microlensing parameters and the confidence contours of MCMC-derived parallax and orbital motion parameters for the same model and MCMC analysis.

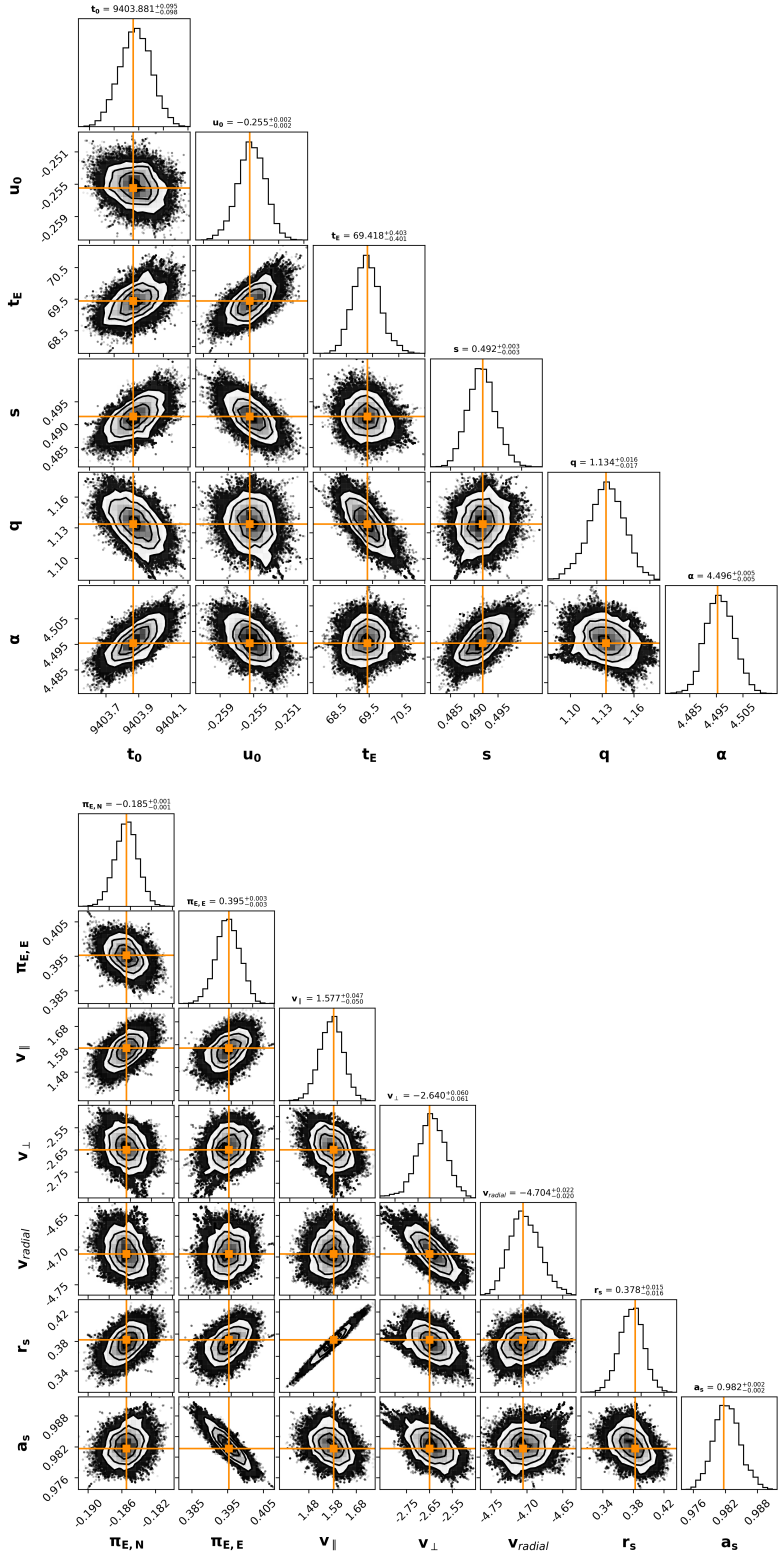


Fig. B.1. Confidence contours in χ^2 space for the MCMC-derived binary-lens microlensing parameters (top) and microlens parallax and orbital motion parameters (bottom) of the best model including orbital motion. The 1σ, 2σ, and 3σ regions are shown in black, dark grey, and light grey shading. Samples lying beyond the 3σ boundary are plotted as black points. The best-model parameters (see Table 3) are indicated by the orange lines and squares. The visualisation was produced with the `corner` package (Foreman-Mackey 2016).